LA-13761-MS
Approved for public release; distribution is unlimited.

Applying the LANL Statistical Pattern Recognition Paradigm for Structural Health Monitoring to Data from a Surface-Effect Fast Patrol Boat

Los Alamos
NATIONAL LABORATORY

Los Alamos National Laboratory is operated by the University of California for the United States Department of Energy under contract W-7405-ENG-36.

Edited by Ann Mauzy, Group IM-1

Cover photo: *The surface-effect fast patrol boat shown on the cover is a pre-series fast patrol boat built by Kvaerner Mandal in Norway. The fiber optic sensor data analyzed in this report were measured on the boat shown in this figure. These data were acquired as part of a joint research effort between the Norwegian Defense Research Establishment and the Naval Research Laboratory in Washington D.C.*

An Affirmative Action/Equal Opportunity Employer

LA-13761-MS

Issued: January 2001

Applying the LANL Statistical Pattern Recognition Paradigm for Structural Health Monitoring to Data from a Surface-Effect Fast Patrol Boat

Hoon Sohn
Charles Farrar
Norman Hunter
*Keith Worden**

**University of Sheffield, United Kingdom*

Los Alamos
NATIONAL LABORATORY

Los Alamos, New Mexico 87545

TABLE OF CONTENTS

APPLYING THE LANL STATISTICAL PATTERN RECOGNITION PARADIGM FOR STRUCTURAL HEALTH MONITORING TO DATA FROM A SURFACE-EFFECT FAST PATROL BOAT

Hoon Sohn, Charles R. Farrar, Norman F. Hunter, and Keith Worden

ABSTRACT

This report summarizes the analysis of fiber-optic strain gauge data obtained from a surface-effect fast patrol boat being studied by the staff at the Norwegian Defense Research Establishment (NDRE) in Norway and the Naval Research Laboratory (NRL) in Washington D.C. Data from two different structural conditions were provided to the staff at Los Alamos National Laboratory. The problem was then approached from a statistical pattern recognition paradigm. This paradigm can be described as a four-part process: (1.) operational evaluation, (2.) data acquisition & cleansing, (3.) feature extraction and data reduction, and (4.) statistical model development for feature discrimination. Given that the first two portions of this paradigm were mostly completed by the NDRE and NRL staff, this study focused on data normalization, feature extraction, and statistical modeling for feature discrimination. The feature extraction process began by looking at relatively simple statistics of the signals and progressed to using the residual errors from auto-regressive (AR) models fit to the measured data as the damage-sensitive features. Data normalization proved to be the most challenging portion of this investigation. A novel approach to data normalization, where the residual errors in the AR model are considered to be an unmeasured input and an auto-regressive model with exogenous inputs (ARX) is then fit to portions of the data exhibiting similar waveforms, was successfully applied to this problem. With this normalization procedure, a clear distinction between the two different structural conditions was obtained. A false-positive study was also run, and the procedure developed herein did not yield any false-positive indications of damage. Finally, the results must be qualified by the fact that this procedure has only been applied to very limited data samples. A more complete analysis of additional data taken under various operational and environmental conditions as well as other structural conditions is necessary before one can definitively state that the procedure is robust enough to be used in practice.

1 INTRODUCTION

This report summarized the analysis of test data obtained from the Naval Research Laboratory (NRL), www.nrl.navy.mil. Based on conversations with the staff from NRL (Mike Todd, miketodd@ccs.nrl.navy.mil) at the 2000 International Modal Analysis Conference, staff at Los Alamos National Laboratory (LANL) volunteered to apply some of the LANL pattern recognition techniques developed for structural health monitoring to data obtained from a surface-effect fast patrol boat shown in Figure 1. The surface-effect ship is a pre-series fast patrol boat built by Kvaerner Mandal in Norway. Together with a research team from the Norwegian Defense Research Establishment (NDRE), the ship designers determined the optimal sensor placement. The sensor installation and data acquisition during sea trials were performed jointly by NDRE and NRL. The boat and the associated data acquisition are summarized in Johnson et al. (2000), Pran et al. (2000), Jensen et al. (2000), and Wang et al. (2000).

Figure 1: Surface-effect fast patrol boat.

As with all structural health monitoring activities, the LANL staff views this problem in terms of a statistical pattern recognition paradigm. This paradigm can be described as a four-part process: (1.) operational evaluation, (2.) data acquisition & cleansing, (3.) feature extraction & data reduction, and (4.) statistical model development for feature discrimination.

Operational evaluation answers four questions regarding the implementation of a structural health monitoring system: (1.) How is damage defined for the system being monitored? (2.) What are the conditions, both operational and environmental, under which the system to be monitored functions? (3.) What are the limitations on acquiring data in the operational environment? and (4.) What are the economic and/or life safety motives for performing the monitoring? Operational evaluation begins to define why the monitoring is to be done and begins to tailor the monitoring to unique aspects of the system and unique features of the damage that is to be detected.

The data acquisition portion of the structural health monitoring process involves selecting the types of sensors to be used, the locations where the sensors should be placed, the number of sensors to be used, and the data acquisition/storage/transmittal hardware. Other considerations that must be addressed include how often the data should be collected, how to normalize the data, and how to quantify the variability in the measurement process. Data cleansing is the process of selectively choosing data to accept for, or reject from, the feature selection process. Filtering and data decimation are two of the most common methods for data cleansing.

The area of the structural health monitoring that receives the most attention in the technical literature is feature extraction. Feature extraction is the process of identifying damage-sensitive properties, derived from the measured vibration response, which allows one to distinguish between the undamaged and damaged structure. Almost all feature extraction procedures inherently perform some form of data compression. Data compression into feature vectors of small dimension is necessary if accurate estimates of the feature's statistical distribution are to be obtained.

Statistical model development is concerned with the implementation of the algorithms that analyze the distribution of extracted features in an effort to determine the damage state of the structure. The algorithms used in statistical model development fall into the three general categories: 1. Group Classification, 2. Regression Analysis, and 3. Outlier Detection. The appropriate algorithm to use will depend on the ability to perform *supervised* or *unsupervised* learning. Here, supervised learning refers to the case where examples of data from damaged and undamaged structures are available. Unsupervised learning refers to the case where data are only available from the undamaged structure (Bishop, 1995).

The Norwegian Defense Research Establishment and NRL undertook this structural health monitoring study. Therefore, it is assumed that they have addressed issues such as the economic and/or life safety motives for performing the monitoring. At present, the LANL staff does not know how damage is defined for the boat. The data are assumed to have been acquired in widely varying operational conditions including varying sea states, varying ship speeds, and varying thermal environments. The limitations, if any, on acquiring data in these operational environments are unknown to the LANL staff.

Data acquisition was also performed by the staff of NDRE and NRL. Therefore, the number, type, and locations of sensors along with the data acquisition/storage/transmittal hardware and data sampling parameters were all established by NDRE and NRL. Fiber optic strain gauges with Bragg gratings were used to measure the dynamic response of the ship. A schematic diagram of the fiber optic sensors is shown in Figure 2. The sensors were distributed through the ship as shown in Figure 3. Three strain time-histories were received from NRL. It was explained that these time histories were measured with the same sensor when the ship exhibited two different structural conditions. However, the LANL staff was not told which sensor these data came from. The first two signals, referred to as Signal 1 and Signal 2, hereafter, were measured when the ship was in "Structural Condition 1" while Signal 3 was measured when the ship was in "Structural Condition 2." The LANL staff was not informed of any data cleansing or data normalization that was performed before the transmission of these signals to LANL. It is assumed that these data were acquired under varying environmental and operational conditions. Changing environmental conditions can include varying sea states and thermal environments associated with the water and air. The variations of operational conditions include ship speed and the corresponding changes in engine performance, mass associated with varying ship cargo, ice buildup and fuel levels, and maneuvers that the ship undergoes. No measures of these environmental or operational conditions were provided.

Given that the first two portions of the statistical pattern recognition paradigm have mostly been completed, this study focused on data normalization, feature extraction, and statistical modeling for feature discrimination. The goal of this investigation was to normalize these data and extract the appropriate features such that Signal 3 could be discriminated from Signals 1 and 2. Also, the same procedure should not discriminate Signal 1 from Signal 2. This report will now summarize the procedures used to obtain these goals.

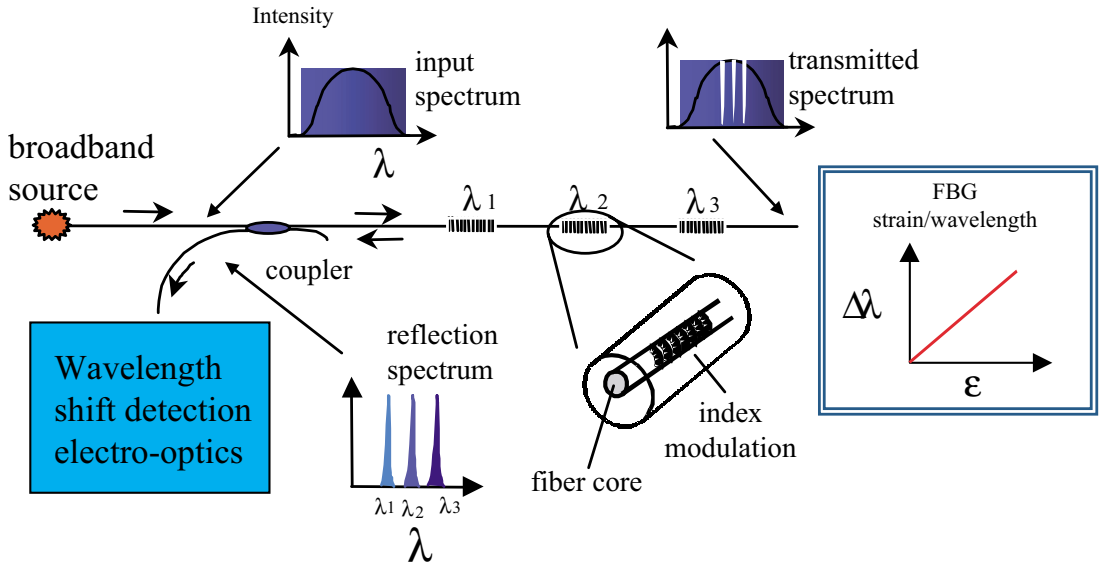

Figure 2: Fiber optic strain gauge with Bragg grating.

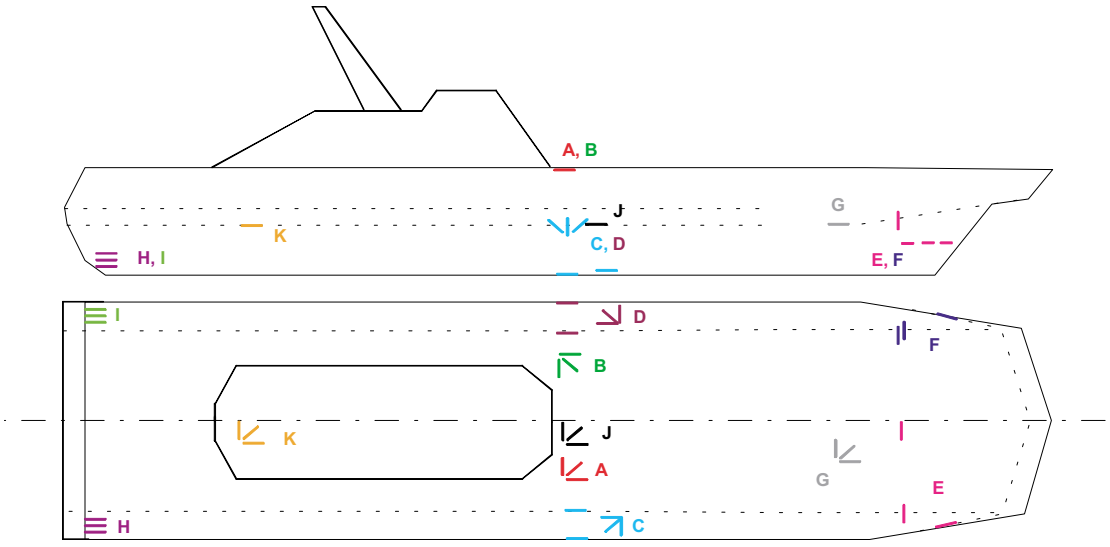

Figure 3: Location of fiber optic strain gauges.

2 DATA ANALYSIS

2.1 The Raw Time Series

First, the raw time series are plotted in Figure 4 to get some intuitive feeling for the signals. A few observations could be made based on this figure: (1) All the signals have "spiky" responses with an occasional large amplitude strain measurement, (2) the amplitude of one signal is not consistent with the amplitude of the other signals indicating the need for data normalization, and (3) significant "skewness" is found in Signal 2. To support some of these observations, the first four statistical moments of the raw time series are summarized in Table 1.

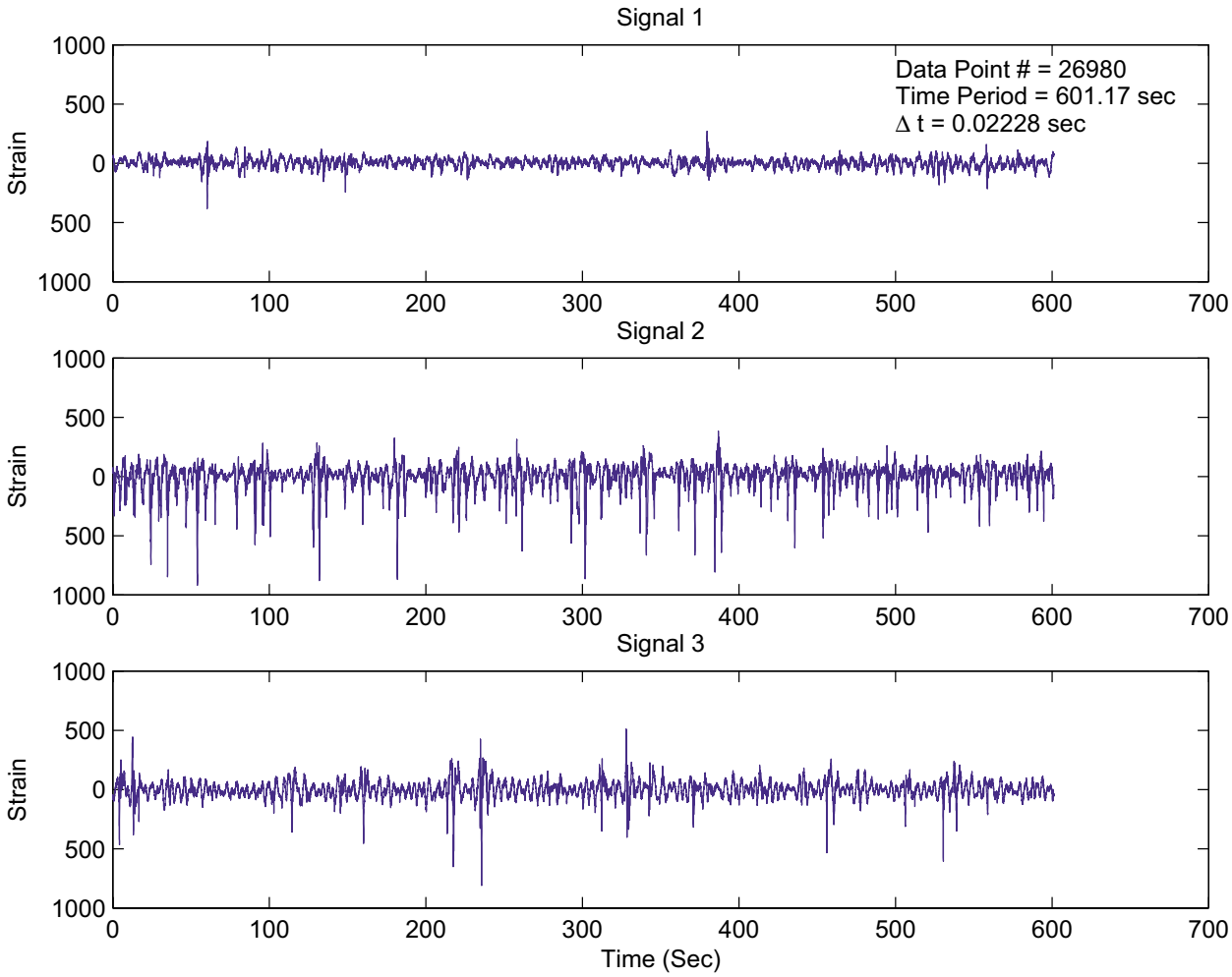

Figure 4: The raw strain time series.

Table 1: Basic statistics of the raw time series amplitudes.

Time Series	Mean Amplitude	Amplitude STD	Skewness	Kurtosis
Signal 1	3.7809	37.7433	-0.4811	6.0854
Signal 2	-0.8207	107.8089	-2.2310	12.6311
Signal 3	-0.7559	74.1260	-0.8134	11.9437

A close look at Table 1 further reveals important facts regarding the data. The sample mean and standard deviation (STD) of one time series are quite different from those of the other signals. Therefore, it seems necessary to conduct some form of data normalization or standardization before doing any statistical model development.

Skewness is a measure of the asymmetry of the data around the sample mean and is defined as

$$s = \frac{\mathrm{E}(x-\mu_x)^3}{\sigma_x^3} \quad , \tag{1}$$

where μ_x and σ_x are the mean and standard deviation of the random variable x, respectively. E(x) is the expectation of random variable x. If the skewness is negative, the data are skewed toward the negative direction of the mean. If the skewness is positive, the data have heavier tails to the positive direction of the mean. The skewness of any perfectly symmetric distribution such as a normal distribution is zero. Signal 2 has a skewness value of -2.2310, which is much larger than the other two signals. The skewness value for Signal 2 indicates that there are more frequent negative strain values than positive ones as can be seen in Figure 4. Therefore, it is suspected that there must have been additional operational and/or environmental effects during the acquisition of Signal 2, not present during the acquisition of Signal 1.

Kurtosis quantifies the relative amount of data located in the tails of a distribution, and the kurtosis of a distribution is defined as

$$k = \frac{\mathrm{E}(x-\mu_x)^4}{\sigma_x^4} \quad . \tag{2}$$

The kurtosis of a theoretical normal distribution is always 3. Distributions with kurtosis greater than 3 have more “mass” in the tails than a normal distribution, and distributions with kurtosis less than 3 have shorter tails than a normal distribution. The last column of Table 1 shows that all three

signals have relatively large kurtosis values (larger than 6) indicating that they all have relatively heavy tails. Therefore, it might be necessary to eliminate outliers corresponding to unusual environmental and operational conditions *a priori*.

2.2 Principal Component Analysis of Moment Statistics

Principal component analysis is a classical method of multivariate statistics, and its theory and use are documented in many textbooks from that field (e.g., Sharma, 1996). Only the briefest description will be given here. Given N samples of data in p-dimensions (x_1, x_2, …, x_p), the principal components analysis (PCA) seeks to project the data into a new p-dimensional set of Cartesian coordinates (z_1, z_2, …, z_p) by a linear transformation.

Calculation is as follows: given data $\mathbf{x}_i=[x_{1i}\ x_{2i}\ x_{pi}]^{\mathrm{T}}$, i= 1, …, N, form the covariance matrix $\sum$,

$$\mathbf{\Sigma} = \sum_{i=1}^{N} (\mathbf{x}_i - \bar{\mathbf{x}})(\mathbf{x}_i - \bar{\mathbf{x}})^{\mathrm{T}} \quad , \tag{3}$$

and decompose $\mathbf{\Sigma}$ so

$$\mathbf{\Sigma} = \mathbf{V}\,\mathbf{\Lambda}\,\mathbf{V}^{\mathrm{T}} \quad , \tag{4}$$

where Λ is a diagonal matrix containing the ranked eigenvalues of $\mathbf{\Sigma}$, and V is the matrix containing the corresponding eigenvectors. (singular value decomposition can be used for this step.) The transformation to principal components is then

$$\mathbf{z}_i = \mathbf{V}^{\mathrm{T}} (\mathbf{x}_i - \bar{\mathbf{x}}) \quad , \tag{5}$$

where $\bar{\mathbf{x}}$ is a mean vector of x_i's. The result of this transformation is that the coordinates z_i are the projection of the original x_i onto the eigenvectors of $\mathbf{\Sigma}$. These eigenvectors are called the *principal components*, and the z_i are called the *scores*.

The new coordinates have the following properties: the z_i's are uncorrelated, and the covariance matrix of the z_i-coordinates is diag[σ_1^2, σ_2^2, …, σ_p^2]. Here $\sigma_1^2 \geq \sigma_2^2 \geq \ldots \geq \sigma_p^2$. Thus, z_1 is the linear combination of the original x_i's with *maximum* variance σ_1^2, z_2 is the linear combination that explains most of the remaining variance σ_2^2, and so on. It should be clear that if the p-coordinates are actually a linear combination of $q < p$ variables, the projections onto the first q principal components will completely characterize the data, and the remaining p-q projections or scores will be zero. In

practice, because of measurement uncertainty, the scores will all be non-zero, and the user should select the number of *significant* components for retention.

Considered as a means of dimension reduction then, PCA works by discarding those linear combinations of the data that contribute least to the overall variance. There are two main applications. First, the technique can provide an effective means of *feature extraction*, i.e., the salient information in the data can be retained while passing to a representation of the data in a reduced dimension. Second, the technique can provide an effective means of *visualizing* the data. If the reduced space has a dimension of 3 or less, the reduced data can be plotted in a form that displays relationships between the points. In the reduced-dimensional space, structure such as clusters may be visualized reflecting the distribution of data in the original higher dimensions.

In order to illustrate the process, consider the features discussed in the last section—the first four moments of the given time-series. The data for visualization were accumulated as follows. First, the data were decimated (an anti-aliasing filter was applied), and three records of time series of length 2698 were obtained. A time window of 1000 points was moved through the records with a step of 8 points. For each window, the first four moments of the time series were evaluated: mean, standard deviation, skewness, and kurtosis. For each signal this process gave 213 4-dimensional feature-vectors, which were concatenated and decomposed using PCA. After the transformation in Equation (5), the projections onto the first two principal components were extracted. The results are plotted in Figure 5.

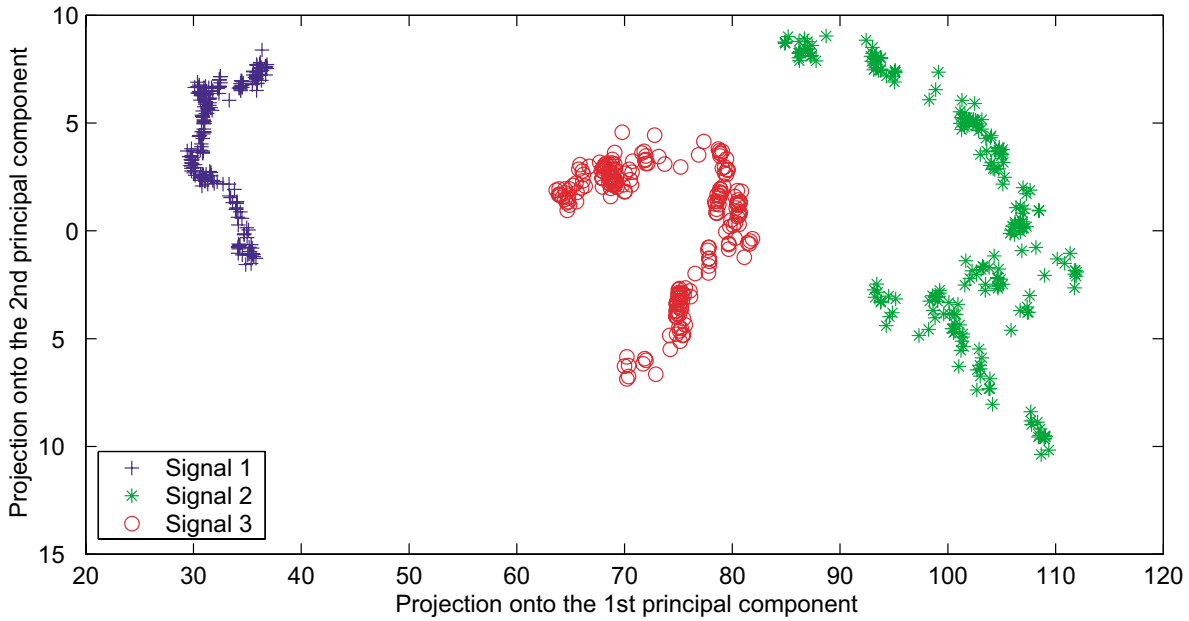

Figure 5: Moment statistics for Signals 1 to 3 projected onto the first two principal components.

The visualization of the moment data shows two striking characteristics. First, the features corresponding to the three signals are separable in the two-dimensional projection. Because PCA is a linear orthogonal transformation, it preserves the distances between data points, and hence the data must be separable in the original four-dimensional space. Second, the features for Signal 3 sit between those for Signals 1 and 2, which correspond to Structural Condition 1. It is this second observation that eliminates the moment statistics as useful features. Because Signals 1 and 2 clearly do not represent the full operational and environmental range of Structural Condition 1, the clusters corresponding to Signals 1 and 2 are disjointed. If data were collected spanning the full range of normal operational and environmental conditions, the features from these data would be expected to interpolate between the features of Signals 1 and 2, and would overlap substantially with those of Signal 3. This observation is not conclusive as the full normal condition data could avoid the features from Signal 3 in the full four-dimensional space. However, PCA shows that because 90% of the full data variance was encapsulated in the first two components, the three separated clusters are nearly coplanar in the four-dimensional space.

This example illustrates the two possible uses of PCA. The two-dimensional visualization shows the existence of separable clusters. In the absence of further information, it would be possible to design or train a classifier that would separate unambiguously Structural Condition 1 from Structural Condition 2 in the two-dimensions—thus feature selection would appear to be possible. In fact, as it is known that the normal condition data here (Signals 1 and 2) are not representative of all environments, the disposition of the three clusters effectively eliminates the moment values as features for novelty detection[1]. Note that these conclusions are only tenable because damage data are available. If true unsupervised learning were required, it would not be possible to eliminate the moments as candidate features.

2.3 Frequency Domain Analysis

Next, the fast Fourier transformation (FFT) of the time signals is computed. Before FFT, the time signals are normalized such that

$$\hat{x} = \frac{x - \mu_x}{\sigma_x} \quad , \tag{6}$$

where $\hat{x}$ is the normalized signal, and μ_x and σ_x are the mean and standard deviation of x, respectively. This normalization procedure is used for all subsequent analyses presented in this report. The

[1] Novelty detection is the lowest level of damage identification, and seeks simply to identify if a new data set is consistent with data corresponding to the previously observed normal conditions.

results of FFT are shown in Figure 6, Figure 7, and Figure 8. Note that because the frequency amplitudes are negligible after 5 Hz, only the range of 0–5Hz is shown here although the Nyquist frequency is 22.44Hz. While Figure 6 shows the FFT of the normalized raw time series without applying any windowing, a Hanning window is applied to the time series before the computation of FFT shown in Figure 7. For the FFT results shown in Figure 8, the time series are divided into 24 segments with 50% overlapping, a Hanning window is applied to each individual segment prior to FFT, and the averaging of 24 FFTs is conducted. There exist noticeable differences among the FFT amplitudes of signals in the range of 0–0.5Hz. However, based on visual inspection of Figure 6, Figure 7, and Figure 8, it is difficult to qualitatively discern any consistent difference between Signals 1 and 2 (Structural Condition 1) and Signal 3 (Structural Condition 2).

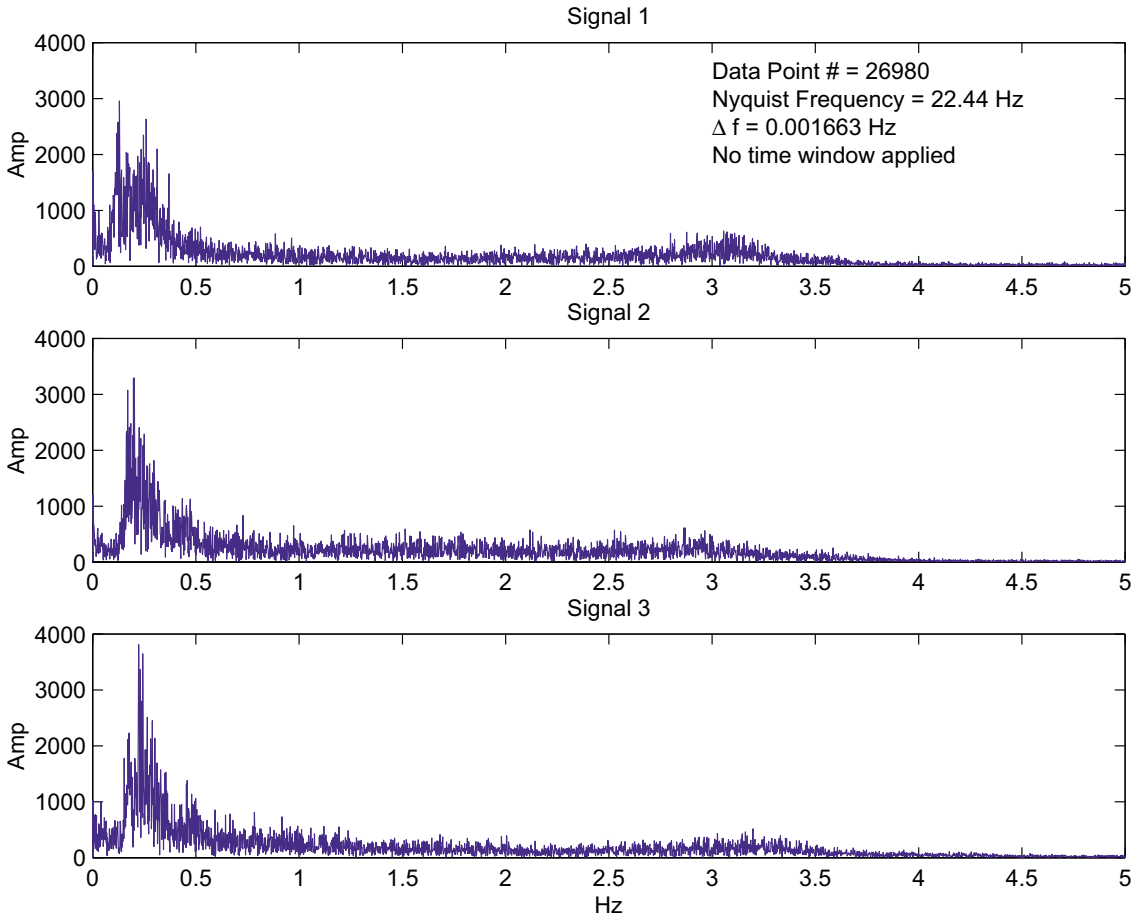

Figure 6: Fourier transform of the raw time series.

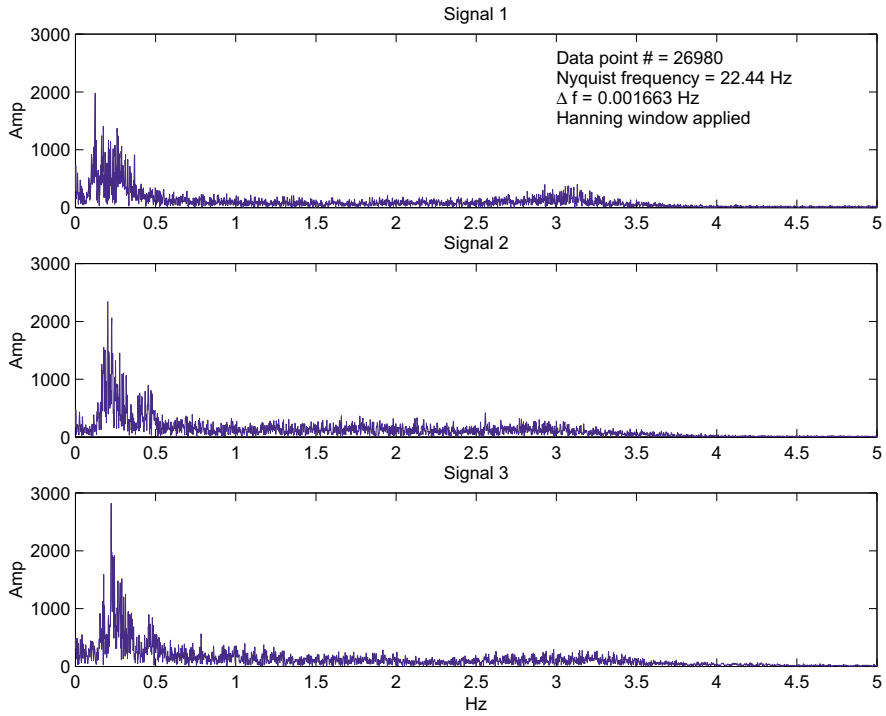

Figure 7: Fourier transform of the time series after applying a Hanning time window.

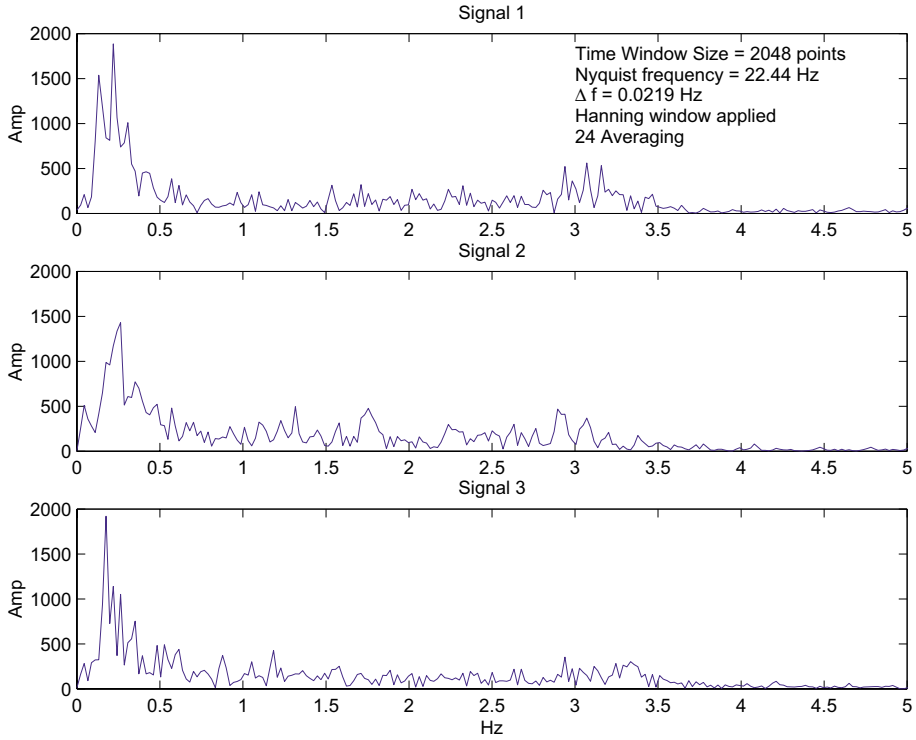

Figure 8: Averaged Fourier transform of the time series.

2.4 Probability Density Estimation

The probability density function (PDF) of an individual time signal is estimated by a kernel density estimation technique (Silverman, 1986). Kernel density estimation can be motivated by observing that if X is a random variable with density function $f(x)$, then $(2h)\cdot f(x) \approx \Pr(x-h<X<x+h)$ or $f(x) \approx (1/2h)\Pr(x-h<X<x+h)$. As h goes to 0 this approximation becomes equality. For a given value of h, the probability of being in the interval $(x-h,x+h)$ can be estimated as the proportion of observed data in the interval. A natural estimate of the density is

(7)

This is referred to as the naïve estimator of $f(x)$. By defining a kernel function $K(x)$ as

$$\int_{-\infty}^{\infty} K(x)\,dx = 1 \quad . \tag{8}$$

the kernel estimator with kernel K is defined by

$$\hat{f}(x) = \frac{1}{nh}\sum_{i=1}^{n} K\left(\frac{x - X_i}{h}\right) \quad . \tag{9}$$

The parameter h is the window width, also called the smoothing parameter or the bandwidth. Just as the naïve estimator can be thought of as a sum of boxes placed over the observations, the kernel estimator can be thought of as a sum of "hills" placed over the observations. In this study, a

Gaussian kernel is used. That is, $K(x) =$.

The quality of the estimate depends critically on two factors. The first is the size of the training set. Discussions can be found in Silverman, (1986) or Scott (1992). Following Silverman's criteria for a univariate density, there are no problems here with the amount of data. The other factor of importance is the value of the smoothing parameter h. If h is too small, the PDF will contain a lot of spurious local structure. If h is too large, the estimate will be over-smoothed, and its decay rate with x will be underestimated. The immediate effect of the latter for structural health monitoring problems is that the normal condition set will appear to be larger than it actually is, and any density-based damage diagnostic may therefore suffer from false negatives. As one might expect, there is an optimum value for h and there are a number of ways of estimating it.

The simplest method and the one adopted by the kernel density estimate is *least-squares cross-validation* (Bowman, 1984). This method seeks to minimize the squared error between the density estimate and the true density:

$$J[\hat{p}(x)] = \int [p(x) - \hat{p}(x)]^2 dx \quad . \tag{10}$$

Because the true density $p(x)$ is unknown, Equation (10) is somewhat limited in its usefulness. However, it can be shown under certain conditions (Silverman, 1986) that the value h which minimizes the following equation also minimizes the mean-squared error between $p(x)$ and $\hat{p}(x)$:

$$M_1(h) = \frac{1}{n^2 h} \sum_i \sum_j K^* \left(\frac{x_i - x_j}{h} \right) + \frac{2}{n h} K(0) \quad , \tag{11}$$

where $K^*(x) = K^{(2)}(x) - 2K(x)$, $K^{(2)}(x) = \int K(z-x)K(z)dz$, and z is a dummy variable.

The minimization is carried out here using a simple quadratic-fit Newton-type method (Leuenberger, 1989). Any minimization routine requires an initial estimate, and the quality of the final result may depend critically on it. This study follows the guidelines in Silverman (1986) and uses the following procedure. An initial smoothing parameter is chosen, h^*; for a univariate distribution, this parameter is,

$$h^* = 0.9An^{-1/s} \quad , \tag{12}$$

where A = min [standard deviation, interquartile range/1.34]. (There are 4 quartiles, Q1, Q2, Q3, and Q4. Twenty-five percent of the data are below Q1; 50% of the data are below Q2, the median; 75% of the data are below Q3; all the data are below Q4. The interquartile range is a range between Q1 and Q3 implying that 50% of the data will be between Q1 and Q3.) The standard deviation and the interquartile range are computed from the observations. At the least, this choice of h should provide a good starting point.

This estimate depends on the assumption that the true distribution is univariate Gaussian. In cases where the density is expected to be close to Gaussian, i.e., uni-modal and with light tails, the estimate above will often be good enough. If there are major departures from normality, i.e., the density is clearly multi-modal, full cross-validation is needed. There are many other approaches to estimating the smoothing parameter, and a good survey is provided by Wand and Jones (1995). Once h^* is established, the program used here assumes a search interval [$h^*/4$, 2 h^*] and carries out

a minimization of $M_1(h)$ over this interval. The procedure continues by carrying out a coarse search over a mesh of 100 points in order to bracket the minimum, and then minimizes using the quadratic fit procedure.

Figure 9 displays the PDF of the raw time series estimated by the kernel density technique. Before the density is estimated, the time signals are normalized according to Equation (6). Therefore, the median values (the peaks) of the PDFs are placed near zero value in the abscissa. (The mean value of each PDF is zero.) Based on the observation of Figure 9, it is concluded that there exists a noticeable difference between PDFs of Signal 1 and Signal 3. Furthermore, the PDF of Signal 2 seems closer to that of Signal 3 rather than to Signal 1. (Again, note that Signals 1 and 2 are supposed to come from the same structural condition and Signal 3 from the other structural condition.) This observation agrees with the results shown in Table 1. Signal 1 has smaller standard deviation than the other two signals, and the significant skewness of Signal 2 is also spotted as shown in the previous skewness value.

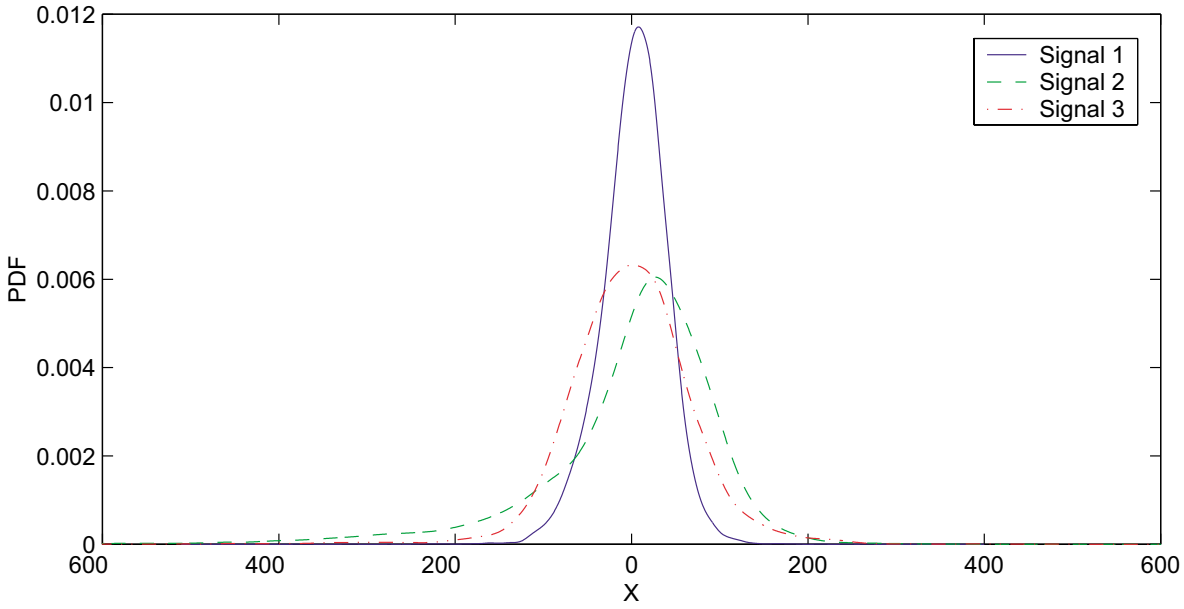

Figure 9: Probability density estimation of signals.

2.5 Statistical Process Control (SPC) Analysis

This section focuses on applying a statistical process control technique known as *a control chart* to the strain measurements. A control chart provides a statistical framework for monitoring future measurements and for identifying new data that are inconsistent with past data (Montgomery, 1997). First, an auto-regressive (AR) model is fit to the strain measurement from Signal 1. The residual error, which quantifies the difference between the prediction from the AR model and the actual measured time history at each time interval, is selected as the damage-sensitive feature for the subsequent control chart analysis. Next, and X-bar chart and an S control chart are employed to monitor the mean and variance of the selected features, respectively. The control limits for the control charts are constructed based on the features obtained from Signal 1. The residual errors computed from the previous AR model and subsequent new data (Signal 2 or Signal 3) are then monitored relative to the control limits. A statistically significant number of features outside the control limits indicate a system transition from Structural Condition 1 to Structural Condition 2.

2.5.1 Auto-Regressive (AR) Model

An AR model with p auto-regressive terms, AR(p), can be written as;

$$x(t) = \sum_{j=1}^{p} \phi_j \, x(t-j) + e(t) \quad , \tag{13}$$

where $x(t)$ is a strain measurement observed at discrete time index t, and $e(t)$ is an unobservable random error (or residual error). In this study the AR coefficients ϕ_j's are estimated by the Yule-Walker method (Brockwell and Davis, 1991).

If the strain measurements are auto-correlated, constructing a control chart that ignores the correlation can lead to charts that give many false alarms and charts that fail to signal when the process being monitored has changed significantly. Because the strain measurements are heavily correlated [see Figure 9 (a)], the auto-correlation is first removed by fitting an AR model to the original strain data. The auto-correlation $\gamma(\tau)$ for $x(t)$ is defined as

$$\gamma(\tau)=\mathrm{E}[x(t)x(t-\tau)] \quad , \tag{14}$$

where τ is the time lag and E[•] denotes the expectation operation. The auto-correlation function in Figure 9 is normalized as follows

$$\rho(\tau) = \frac{\gamma(\tau)}{\gamma(0)} \quad , \tag{15}$$

which implies that $\rho(0) = 1$; $\rho(\tau)$ is often called an auto-correlation coefficient function.

Initially, the order of the auto-regressive process to fit the time series is unknown. This problem is analogous to deciding on the number of independent variables to be used in a multiple regression analysis. If the order of the AR model is appropriately selected and if the time series can be cast as AR model, the residuals from the fit should be nearly uncorrelated with no systematic pattern. There are a variety of techniques for choosing the model order, such as Akaike's Information Criterion (AIC) and partial auto-correlation analysis (Box et al., 1994). In this study, the partial auto-correlation analysis is conducted. An AR(p) model shown in Equation (13) can be rewritten as follows

$$x(t) = \sum_{j=1}^{p} \phi_{pj}\ x(t-j) + e(t) \quad , \tag{16}$$

where ϕ_{pj} denotes the jth coefficient in an auto-regressive representation of order p, so that ϕ_{pp} is the last coefficient of AR(p) with lag p. This quantity, ϕ_{pp}, regarded as a function of lag p, is called the partial auto-correlation function. For an AR process of order p, the partial auto-correlation function will be zero for lags greater than p. However, since the theoretical correlation is unknown, the partial auto-correlation is estimated from the data. This estimated correlation would differ somewhat from its theoretical counterparts. Therefore, the partial auto-correlation of an actual AR(p) will not be exactly zero even after lags greater than p, but they are considered effectively zero if the correlation values are within the blue lines shown in Figure 11. Here, the blue lines represent $2\sigma_{\phi}$ limits of the partial auto-correlations. Assuming that the process is a AR(p) model, the estimated partial auto-correlations of order p+1 and higher, are approximately independent and normally distributed with zero mean and standard deviation σ_{ϕ}. It can be shown that if n is the number of observations used in fitting, $\sigma_{\phi}^2 = 1/n$ (Box et al., 1994). For Signal 1, the partial auto-correlation approaches zero after lag 30. Therefore, AR(30) is selected for the subsequent analyses. Figure 10 (b) demonstrates that after fitting the AR(30) model to Signal 1, the resulting residual errors, $e(t)$, show practically no correlation. The auto-power spectrum of the residual errors shown in Figure 12 provides further evidence that the resulting residual errors are uncorrelated.

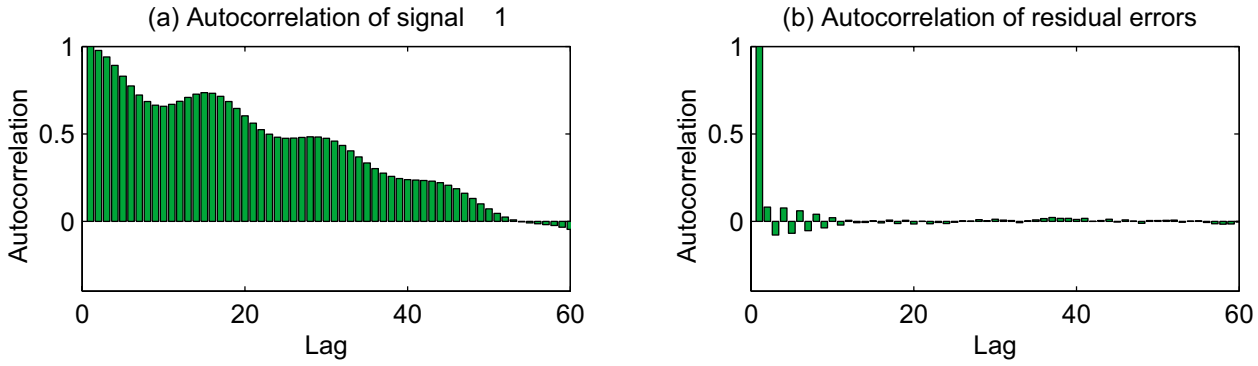

Figure 10: Autocorrelation functions of Signal 1 and the corresponding residual errors.

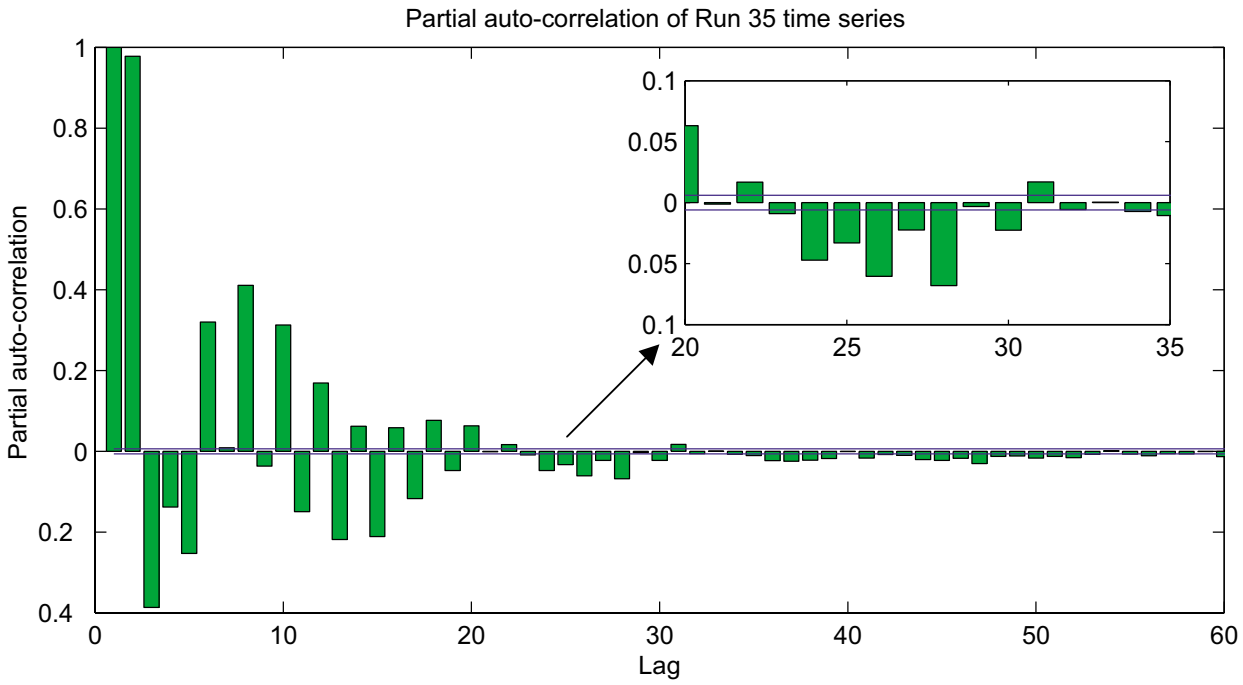

Figure 11: Partial autocorrelation function of Signal 1.

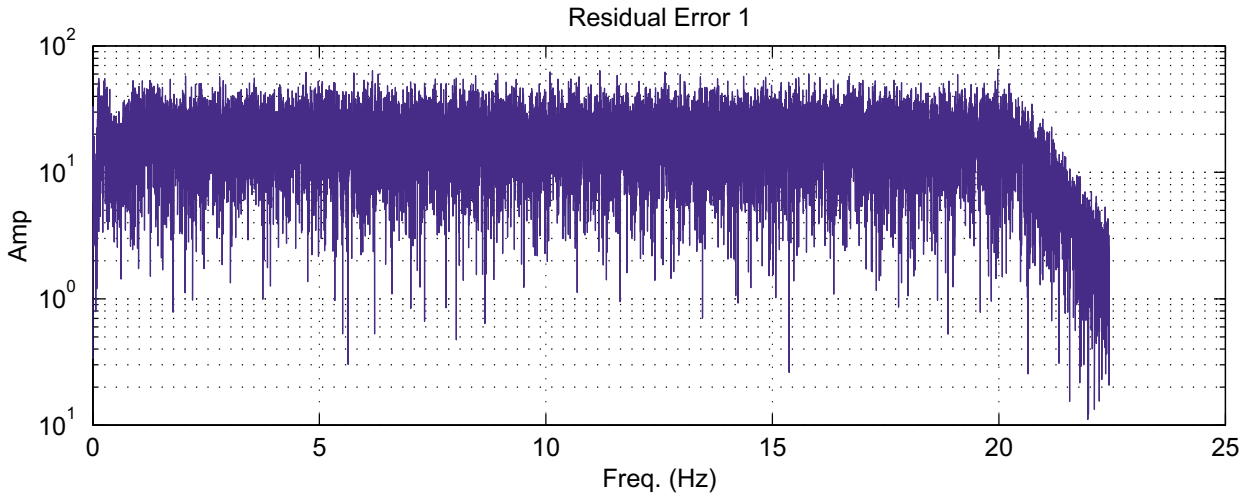

Figure 12: Power spectrum of the residual errors of Signal 1 (Nyquist frequency=22.44Hz, Δf=0.001663Hz, no time window applied, number of data points=26980).

2.5.2 PDF of Residual Errors

In the previous section, the AR model is constructed considering Signal 1 the "baseline" data. When new data become available (for instance, Signal 2 or Signal 3 in this example), the new measurement is predicted using the AR model, whose parameters were estimated from the baseline data. That is, using Equation (13), the current response $x(t)$ of the new data is predicted from its previous responses, and the AR coefficients estimated from the baseline data. If the underlying system has changed, the AR model will no longer fit the new measurements as well, and the probability distribution of the residual errors will vary.

Figure 13 plots the residual errors of Signals 1, 2, and 3. Note that all signals are normalized according to Equation (6) before fitting the AR model to the signals and the AR model is estimated from Signal 1. Comparison of Figure 4 and Figure 13 reveals that residual errors are closer to a random process than the actual strain measurement, and most of the skewness is removed during this process. Table 2 summarizes the basic statistics of the residual error time series. More quantitative analysis can be performed by comparing Table 1 and Table 2. Again, the residual errors eliminate most of the asymmetry. However, the kurtosis values of Signals 2 and 3 have increased.

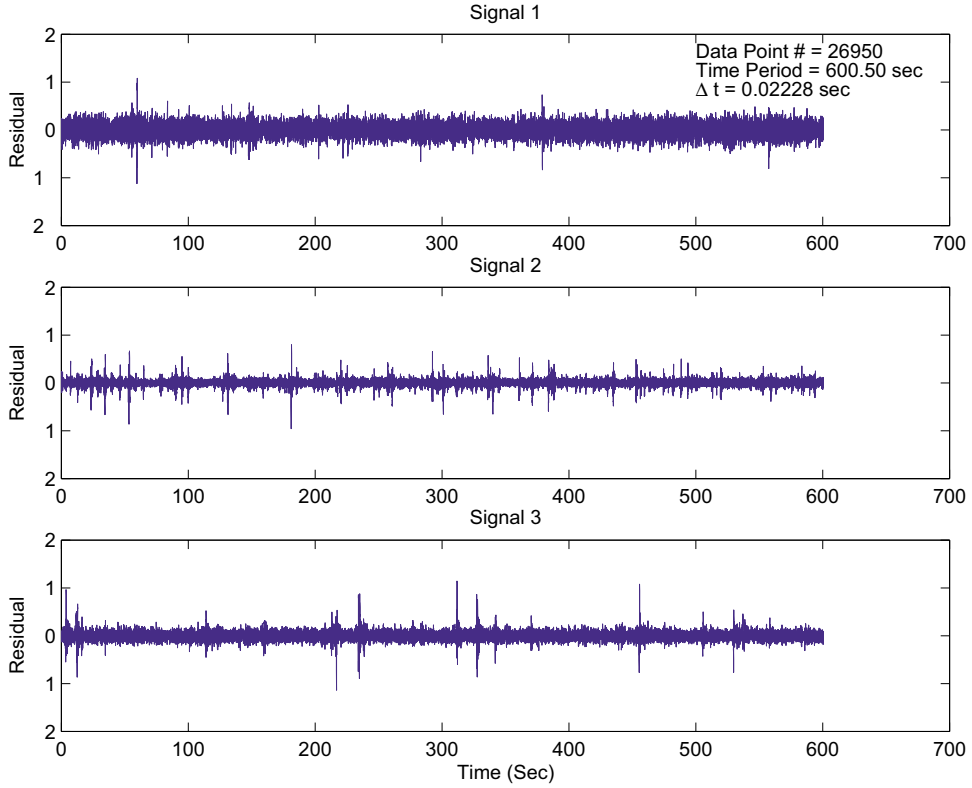

Figure 13: Residual errors of individual signal after fitting an AR(30) model to the signal.

Table 2: Basic statistics of the residual errors

Time Series	Mean	STD	Skewness	Kurtosis
Residual 1	-1.2447e-005	0.1307	-0.0645	4.6419
Residual 2	5.1715e-005	0.0822	-0.3456	14.1446
Residual 3	2.4922e-005	0.0942	0.1050	16.1841

The standard deviations shown in Table 2 reveal that the residual errors of Signal 1 have a larger standard deviation than those of the other two signals. A similar result can be found in Figure 14, where the PDFs of the residual errors have been estimated with the Kernel density procedure. Because the AR model was constructed based on Signal 1, a smaller standard deviation is expected for Signal 1 than the others. Again, it is very unlikely that the residual errors of the training data sets are larger than those of new data sets. This observation caused speculation that the AR model is not fitting the time series well. This issue will be discussed in more detail later in Section. 2.8.

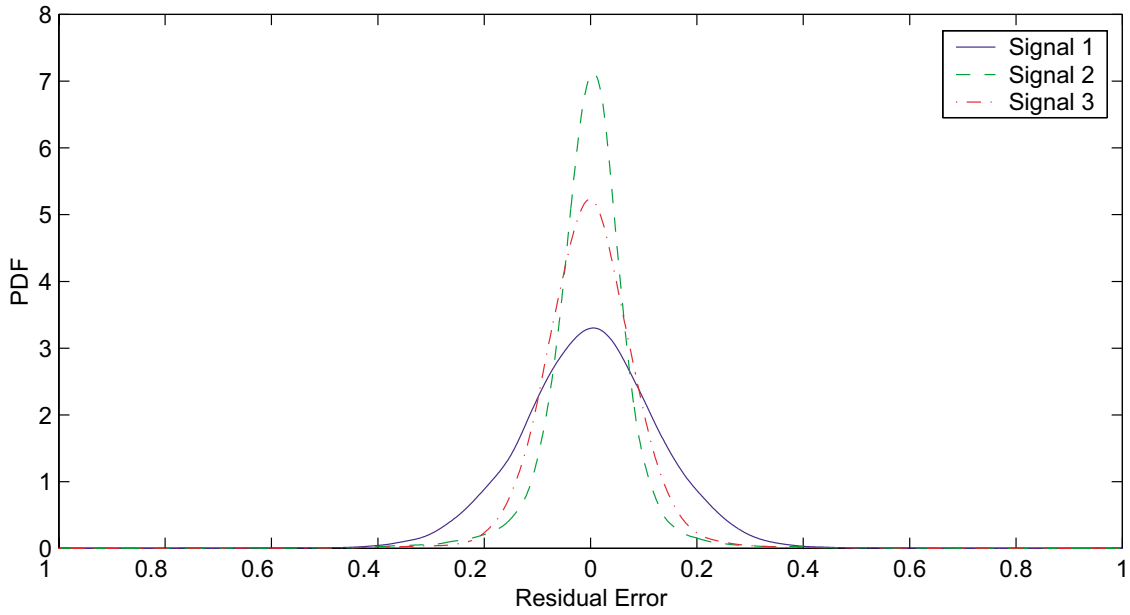

Figure 14: Probability density estimation of residual errors.

2.5.3 Control Chart Analysis of Residual Errors

In Section 2.5.1 AR coefficients are first estimated by fitting an AR model to the time series of Signal 1 using the Yule-Walker method (Box et al. 1994). Then, an investigation is made to determine how this AR model can predict or reproduce Signals 2 and 3. The residual error is defined as the difference between the newly obtained time series (in this example, either Signal 2 or

Signal 3) and the prediction of these time series obtained from the AR model. This residual error is used as the damage-sensitive feature for the subsequent control chart analysis. The basic premise of this approach is, "If the system has been changed since the AR model was constructed, this AR model will no longer be able to predict or reproduce the newly measured time series, thus causing changes in the probability distribution of the residual error." That is, when the system of interest experiences abnormal conditions, the mean and/or variance of the extracted features are expected to change. To monitor these changes in the density function, a control chart analysis is employed here. In this study, X-bar and S control charts are employed to monitor the mean and variation changes of the selected feature and to identify data points that are inconsistent with the past data sets. Several variations of the control chart analyses can be found in Montgomery, 1997.

Control limits are constructed using the baseline data (the residual errors from Signal 1). Then, when a new data set becomes available, the new response data are predicted, and the residual errors are computed. When the plotted mean or variation value of the residual error goes beyond the control limits, it is concluded that something has changed with the structure. A brief description of X-bar and S control charts are described below. A more detailed explanation regarding the application of control chart analysis to damage diagnosis can be found in Sohn et al., 2000.

To monitor the mean variation of the features using the X-bar control chart, the features are first arranged in subgroups. The elements of each subgroup are designated τ_{ij} (i=1,..., q and j=1,..., p). Here, τ_{ij} is the extracted feature from the previous section, *i.e.*, the residual errors. The value q is the number of subgroups, and p is the size of individual subgroup. The subgroup size p is often taken to be 4 or 5 (Montgomery, 1997). If p is chosen too large, a drift present in an individual subgroup mean may be obscured, or averaged-out. An additional motivation for the usage of subgroups, as opposed to individual observations, is that the distribution of the subgroup mean values can be reasonably approximated by a normal distribution as a result of central limit theorem (Montgomery, 1997). Next, the subgroup mean $\overline{X}_i$ and standard deviation S_i of the features are computed for each subgroup (i = 1,..., q):

$$\overline{X}_i = mean(\tau_{ij}) \quad \text{and} \quad S_i = std(\tau_{ij}) \quad , \tag{17}$$

where the mean and standard deviation are computed with respect to p observations in each subgroup. An X-bar control chart is constructed by drawing a centerline (CL) at the subgroup mean and two additional horizontal lines corresponding to the upper and lower control limits (UCL & LCL) versus subgroup numbers (or with respect to time). The centerline and two control limits are defined as follows:

$$\text{CL} = mean(\overline{\text{X}}_i)\,,\ \text{UCL} = \text{CL} + Z_{\alpha/2}\frac{\text{S}}{\sqrt{q}}\text{, and }\ \text{LCL} = \text{CL} - Z_{\alpha/2}\frac{\text{S}}{\sqrt{q}} \quad , \tag{18}$$

where the calculation of mean is with respect to all subgroups (i = 1,..., q). The value $Z_{\alpha/2}$ is the percentage point of the normal distribution with zero mean and unit variance such that $P[z \geq Z_{\alpha/2}] = \alpha/2$. The variance S^2 is estimated by averaging the variance S_i^2 of all subgroups:

$$\text{S}^2 = mean(\text{S}_i^2) \quad . \tag{19}$$

Note that if $\overline{\text{X}}_\text{i}$ can be approximated by a normal distribution following the central limit theorem, the control limits in Equation (18) correspond to a 100(1-α) % confidence interval. In many practical situations, the distribution of features may not be exactly normal. However, it has been shown that the control limits based on the normality assumption can often be successfully used unless the population is extremely non-normal (Montgomery, 1997). If the system experienced some change, this would likely be indicated by an unusual number of subgroup means outside the control limits; a charted value outside the control limits is referred to as an *outlier* in this study. The monitoring of structural condition changes is performed by plotting $\overline{\text{X}}_i$ values obtained from the new data set along with the previously constructed control limits. In general, the observation of a large number of outliers does not necessarily indicate that the structure is damaged but only that the system has varied to cause statistically significant changes in its vibration signatures. This variability can be caused by a variety of environmental and operational conditions that the system is subject to. If environmental and operational parameters are measured, a multivariate control chart can be developed to account for the variability.

To monitor variability within each subgroup, an S control chart can be constructed in a similar fashion as an X-bar chart. For each subgroup the sample standard deviation of the residuals is computed (S_i in Equation (17)). These sample standard deviations from each subgroup become the charted values. The upper and lower control limits (UCL and LCL) of the S control chart are

$$\text{UCL} = \text{S}\sqrt{\frac{\chi_{1-\alpha/2,q-1}}{q-1}}\ \text{ and }\ \text{LCL} = \text{S}\sqrt{\frac{\chi_{\alpha/2,q-1}}{q-1}} \quad , \tag{20}$$

where $\chi^2_{p,n}$ denotes the pth quartile of a Chi-square random variable with n degrees of freedom, and S is defined in Equation (19). Again, in the examples α was chosen to be 0.01.

The diagnostic results of X-bar and S control chart analyses are plotted in Figure 15 and Figure 16. Again, the X-bar and S control charts monitor the mean and variance changes of the underlying process, respectively. The control charts are constructed using the residual errors obtained from Signal 1 so that the control limits correspond to the 99% confidence interval of a normal distribution. However, a large number of outliers are observed even for Signal 1. Although only about 1% of residual errors are supposed to lie outside the confidence interval, about 2.45% (33 outliers out of 1347 sample points) and 9.13% (123 outliers out of 1347 sample points) of outliers exist for the X-bar and S control charts of Signal 1, respectively. This false-positive warning might be attributed to several facts: (1) The signals are nonstationary and the AR linear prediction model cannot capture the nonstationary nature of the underlying system. (2) As shown Figure 10 (b), the AR model did not completely remove the correlation between lags 1–8. Therefore, the observations within one subgroup are still somewhat correlated, and this underestimates the subgroup standard deviation possibly resulting in false-outliers. The bottom line is that the AR model employed here and the subsequent analysis of the residual errors do not provide a good means of discrimination.

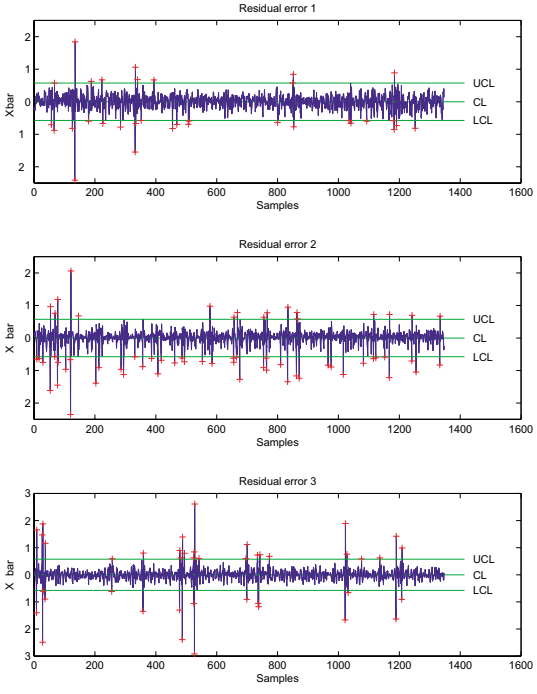

Figure 15: X-bar control chart.

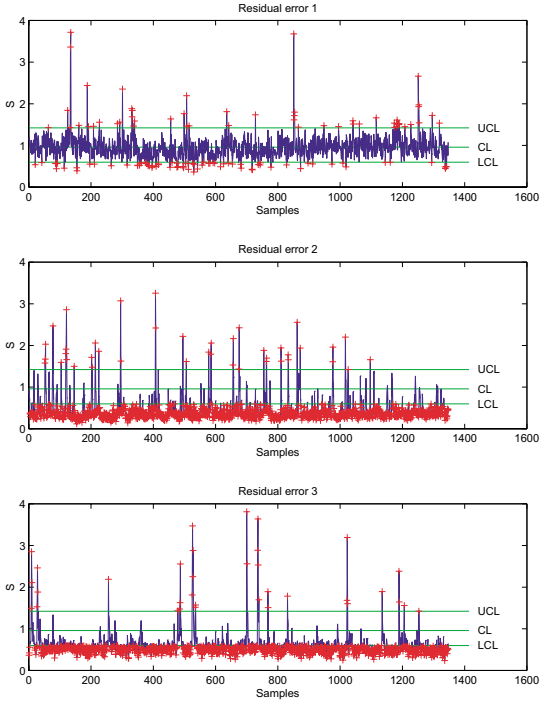

Figure 16: S control chart.

2.6 Bispectrum and Bicoherence Analyses

2.6.1 Definition of Bispectrum and Bicoherence

The power spectrum is the decomposition of signal power in the frequency domain. When this concept is extended to higher orders, the result is called a polyspectrum. More specifically, the third-order polyspectrum is referred to as *bispectrum*. The bispectrum is defined as the frequency decomposition of the skewness, or third-order covariance function, of a signal. The bispectrum provides information regarding such signal features as phase coherence, which is absent in the second-order power spectrum. An important use of the bispectrum is the detection of nonlinearity. Because of its sensitivity to nonlinearity, it is believed that the bispectrum has potential uses in the area of structural health monitoring and damage detection. For example, the bispectrum has been shown to be an indicator of fatigue cracks in cantilever beams (Rivola and White, 1998) and has been applied to damage detection in rotating machinery (Li et al. 1991). Furthermore, higher order measures such as the bispectrum are insensitive to Gaussian noise because the third-order cumulant of such a Gaussian process will yield a zero bispectrum across all frequencies.

First, the third-order covariance (cumulant) function is defined as follows:

$$c_3(k,l) = \mathrm{E}[\,x(t)\;x(t+k)\,x(t+l)\,]\;, \tag{21}$$

where E[·]denotes the expectation operator. For a discrete time series, the discrete bispectrum is defined as the double Fourier transform of the third-order covariance function and can be expressed as:

$$B(f_1, f_2) = \sum_{k=-\infty}^{\infty} \sum_{l=-\infty}^{\infty} c_3(k,l) \exp(-if_1 k) \exp(-if_2 l) \quad . \tag{22}$$

The bispectrum is a function of two different frequencies f_1 and f_2, and only those bifrequencies (f_1, f_2) that fall within the following domain need be computed:

$$f_1 \le f_2, \text{ and } 2f_1 + f_2 \le f_s \tag{23}$$

where f_s is the sampling frequency. This triangular region is referred to as the *Principal Domain*, and all bifrequencies outside of this domain are redundant as a result of the symmetric properties of the bispectrum. A peak in the bispectrum at the bifrequency (f_1, f_2) indicates a coupling between the three frequencies f_1, f_2 and f_3(=f_1+ f_2) and their corresponding phases ϕ_1, ϕ_2 and ϕ_3. This frequency and phase coupling is the result of a quadratic type of nonlinearity within the signal. (The phase coupling will be demonstrated later using numerical examples.)

In practice, a normalization of the bispectrum, referred to as the bicoherence, is commonly used. To normalize the bispectrum, the final estimate is divided by the product of the spectral components:

(24)

where $b(f_{1,}f_2)$ is the bicoherence, and $C_2(f)$ is the Fourier transformation of the following covariance function:

$$c_2(k) = \mathrm{E}[\, x(t)\, x(t+k)\,] \quad . \tag{25}$$

This normalization measures the percentage of power at frequency $f_3(=f_1+f_2)$ caused by wave coupling. The bicoherence removes the dependency on amplitude, or in other words, it is completely independent of the power of the three waves. The bicoherence measures the percentage of power at frequency f_1+f_2 caused by signal coupling of components at f_1 and f_2. The bicoherence takes on an amplitude value between 0 and 1. A value of one indicates that all the energy at f_1+f_2 is from the coupling of components at f_1 and f_2. Therefore, this function can be used to detect the presence of harmonics.

2.6.2 An Example Using a Synthetic Signal

In order to understand the properties of the bispectrum, a synthetic signal consisting of several cosine components was generated. Specifically, sixty-four independent realizations of the signal were generated, each one containing 64 samples:

$$y(t) = \sum_{k=1}^{p}\sum_{i=1}^{3} \alpha_{ki} \cos(2\pi\lambda_{ki}t + \phi_{ki}) + \sum_{k=1}^{q} \beta_k \cos(2\pi\bar{\lambda}_k t + \bar{\phi}_k) \quad . \tag{26}$$

The sample rate was chosen to be 400Hz. One phase coupled triplet (p=1) was chosen at the frequencies (λ_{1i}) of 40Hz, 80Hz, and 120Hz, with amplitudes (α_{1i}) of one. Notice that 40Hz and 80Hz add to 120Hz, and for this reason are said to be frequency coupled. In order to be phase coupled, the phases of the sinusoids must also have the same additive relationship, with ϕ_{11} and ϕ_{12} summing to ϕ_{13}. An additional harmonic for the uncoupled case (terms with an overbar) was chosen at the frequency 160Hz. This frequency of 160Hz was chosen intentionally to form a frequency coupled relationship between 40Hz and 120Hz. However, the corresponding phase of the 160Hz component was chosen randomly, and thus does not exhibit the phase coupling. The bispectrum should only pick up on the terms that are frequency and phase coupled. Note that, while the

bispectrum of a linear time-invariant system is identical to zero, the bispectrum of $y(t)$ in Equation (26) will not vanish because of the presence of a quadratic nonlinearity (quadratic phase coupling) in the system.

In Figure 17, it can be seen that both the bispectrum and the bicoherence reveal the phase and frequency coupling between 40Hz and 80Hz . The bispectrum does not show a peak at 40Hz and 120Hz because of the lack of phase coupling between these two frequency components with the sum component of 160Hz.

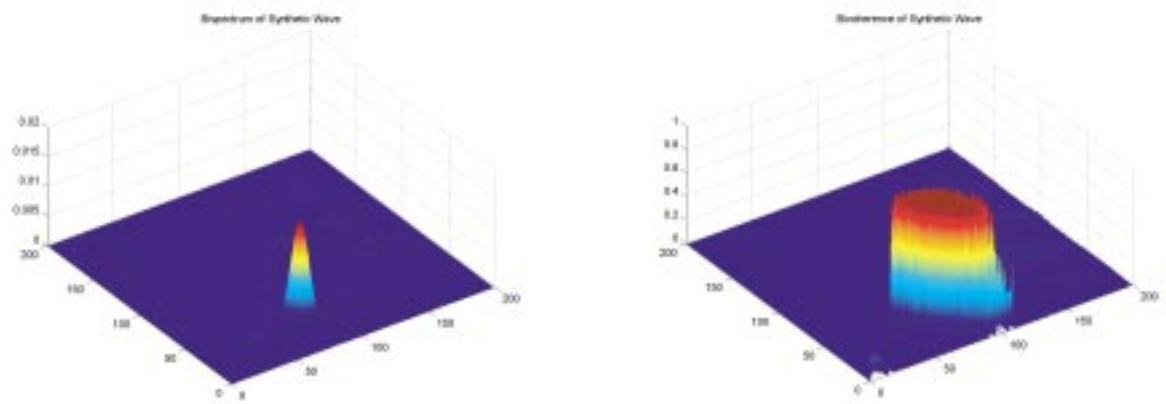

(a) Bispectrum (b) Bicoherence

Figure 17: (a) Bispectrum of synthetic signal, max peak at (40Hz, 80Hz) (b) Bicoherence of synthetic signal, broad peaks centered at (40Hz, 80Hz).

2.6.3 Application to the Strain Measurements

Figure 18 and Figure 19 show the bicoherence analyses of the raw time series. For all signals, some sort of frequency coupling is observed indicating the system nonlinearity. However, the coupling patterns, as shown in Figure 19, significantly vary from one signal to another. Based on the comparison of Figure 18, Figure 19, and Figure 6, the bicoherence produces more distinctions between the signals than the FFTs. However, it is still difficult to group Signals 1 and 2 together in a quantitative manner. Particularly, it is noted that the nonlinearity of Signal 2 is more severe than that of the other two signals. Therefore, given that there is no damage for Signals 1 and 2, it is again doubted that Signal 1 and Signal 2 were recorded under the same operational condition.

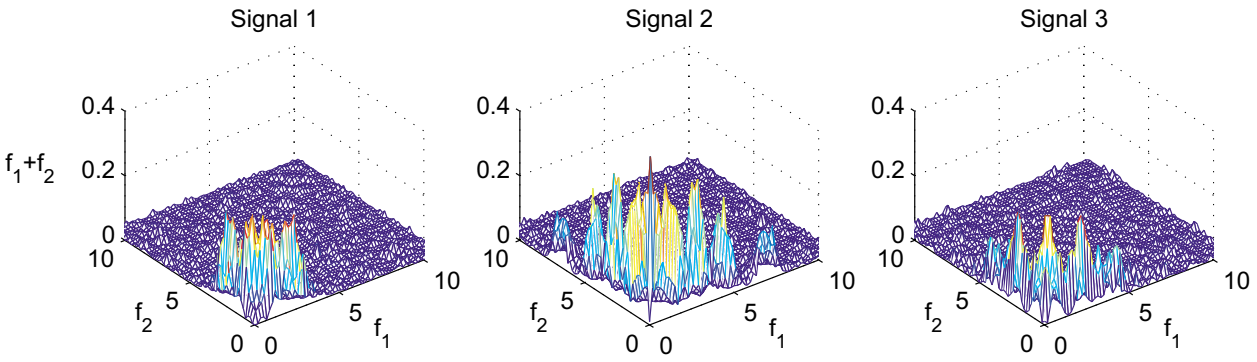

Figure 18: Mesh plots of the bicoherence of the raw time series.

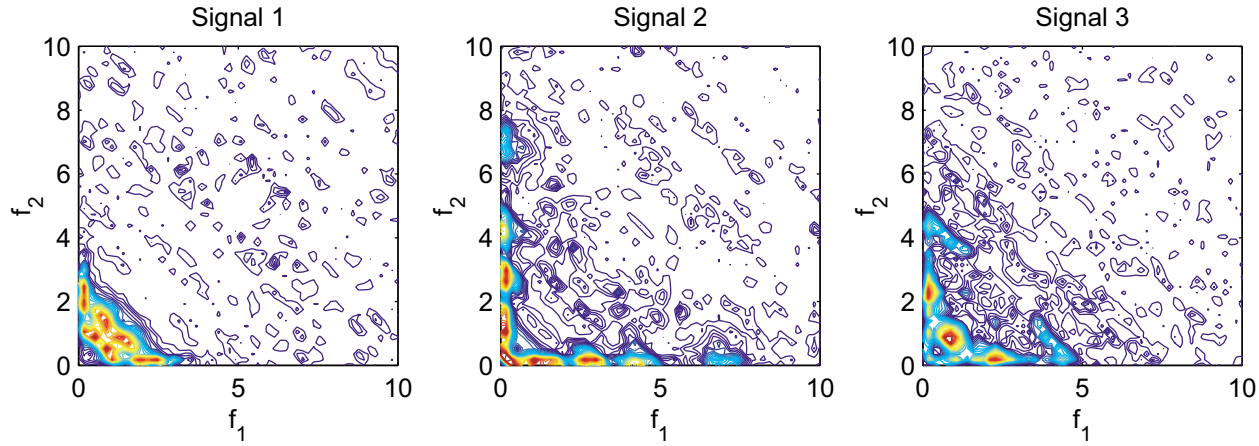

Figure 19: Contour plots of the bicoherence of the raw time series.

Instead of employing the raw time series, similar bicoherence analyses are repeated using the residual errors obtained in Section 2.5.1 The analysis results are reported in Figure 20 and Figure 21. Although results were obtained that are similar to those obtained from the biocoherence analysis of the original time series, the peaks of frequency coupling seem more distributed when the raw time series are analyzed and compared to the biocoherence analysis of the residual errors. It is speculated that because the residual errors are closer to Gaussian noise than the raw time series, the nonlinearity becomes more prominent when the residual errors are employed for the bicoherence analysis. (Again, note that the bicoherence analysis suppresses Gaussian noise processes and detects nonlinearities in signals.)

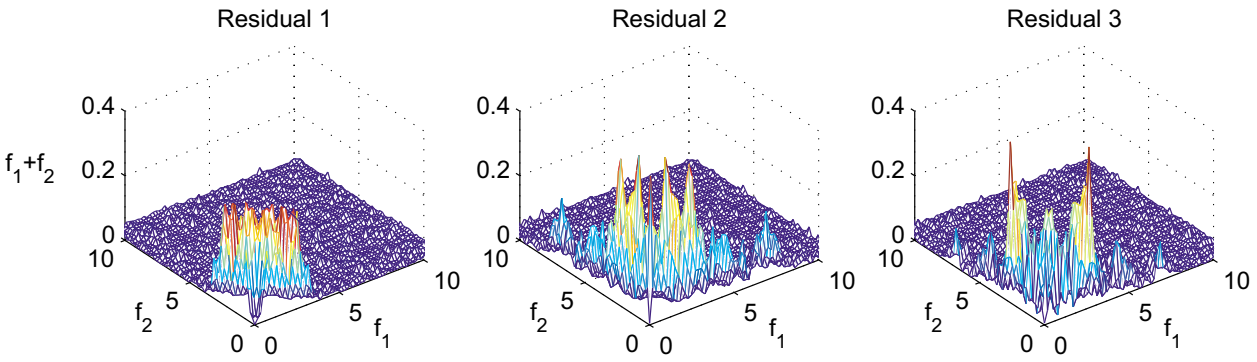

Figure 20: Mesh plots of the bicoherence of the residual errors.

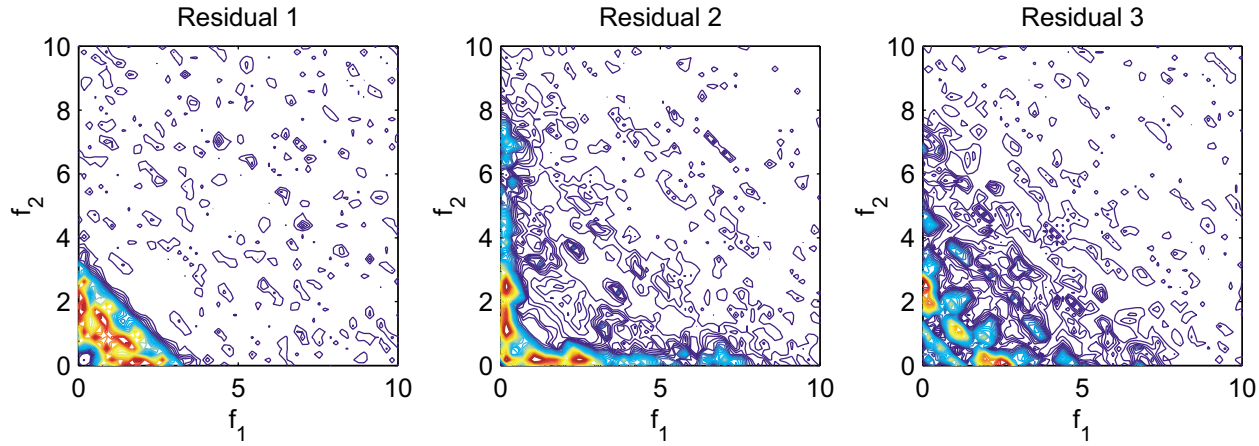

Figure 21: Contour plots of the bicoherence of the residual errors.

2.7 Spectrogram (Time-Frequency) Analysis

2.7.1 Definition of Spectrogram

Spectrogram computes the time-dependent Fourier transform of a signal using a sliding window. This form of Fourier transform is also known as the short-time Fourier transform and it has numerous applications in speech, sonar, and radar processing. The spectrogram first splits the original signal into overlapping segments and applies a time window such as a Hanning window to each segment. Then, it computes the discrete-time Fourier transform of each segment to produce an estimate of the short-term frequency content of the signal over the given time period. Note that for a signal from a time-invariant system, the frequency content should not change with respect to

the time axis. That is, for a linear time-invariant system, it is expected to observe horizontal lines across all time values. For example, consider a simple linear system consisting of four masses and four springs. The response at an arbitrary degree of freedom (DOF) can be represented as

$$y(t) = \sum_{i=1}^{4} \mathrm{A}_i \sin(2\pi f_i t + \phi_i) \quad . \tag{27}$$

If f_i (i=1,…,4) are set to be 5.1Hz, 10.9Hz, 20.6Hz, 40.8Hz, respectively, the spectrogram of $y(t)$ displays four distinct horizontal lines as shown in Figure 22. Here, the phase ϕ_i is determined by the damping of the physical system, and the amplitude A_i is a function of the mode shape properties. In this example ϕ_i and A_i are, however, randomly chosen between ($-\pi$, $+\pi$) and (-1, +1) to simplify the problem.

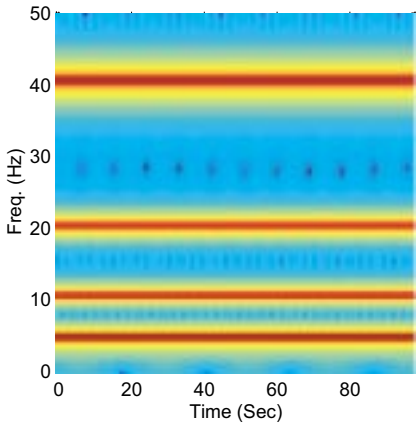

Figure 22: A typical spectrogram of a linear time-invariant (LTI) system response.

2.7.2 A Numerical Example of Time-Frequency Analysis

To better understand the time-frequency analysis using a spectrogram, the spectrogram analysis is applied to a simulated signal with multi-frequency components. A 10-second time signal with frequency components, 0.5Hz, 4Hz, 8Hz, and 30Hz, is generated from the following equation.

$$y(t) = 0.5\sin(2\pi \times 0.5t) + 1.1\sin(2\pi \times 4t) + 1.1\sin(2\pi \times 8t) + 0.2\sin(2\pi \times 30t) \quad . \tag{28}$$

where the time duration of the frequency components are 1–9 seconds, 0–5 seconds, 5–10 seconds, and 2.2–2.5 seconds for 0.5Hz, 4Hz, 8Hz, and 30Hz frequency components, respectively. For example, the first frequency component,$0.5\sin(2\pi \times 0.5t)$, lasts from 1 to 9 seconds. One thousand

twenty-four points are sampled for the 10-second period resulting in Nyquist frequency of 51.2Hz. Figure 23 shows the synthesized signal. Note that a sudden frequency change is noticed around 5 seconds because of a transient from $1.1\sin(2\pi\times 4t)$ to $1.1\sin(2\pi\times 8t)$ in Equation (28). However the signal components corresponding to frequency value 30Hz are difficult to visually detect.

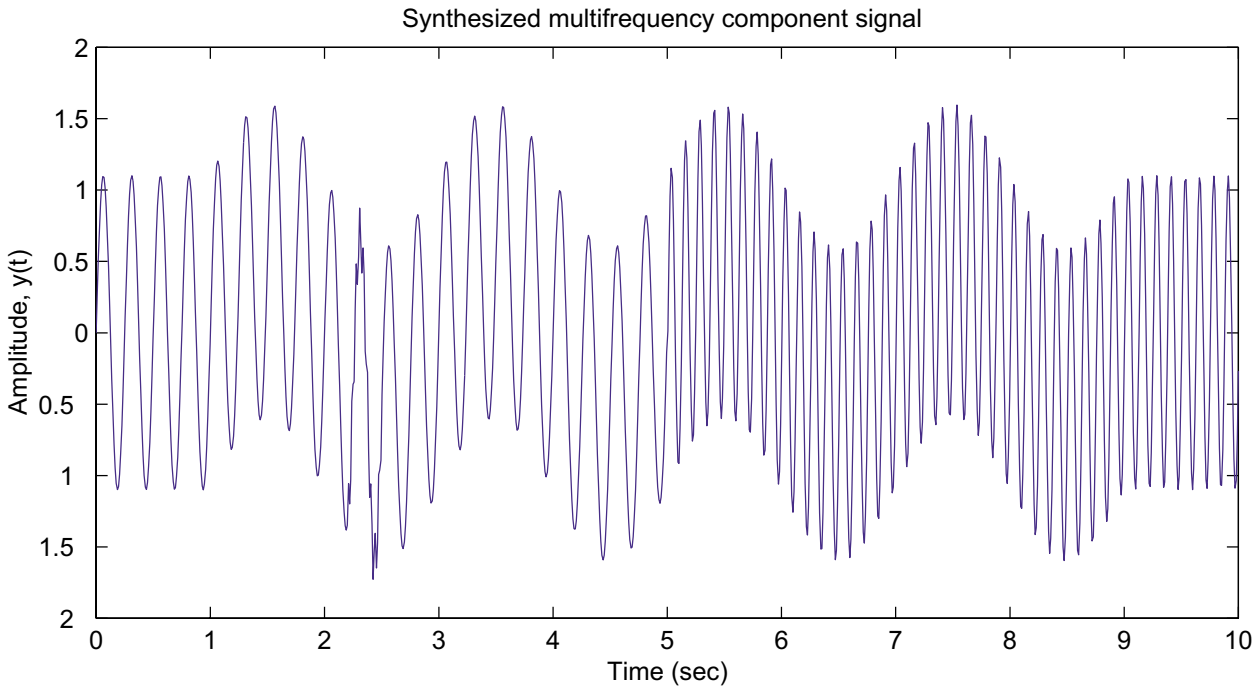

Figure 23: A synthesized signal with multi-frequency components. (Number of data points=1024; $y(t)= 0.5\sin(2\pi\times 0.5t)+1.1\sin(2\pi\times 4t)+1.1\sin(2\pi\times 8t)+2.0\sin(2\pi\times 30t)$. The time durations of each frequency component are 1–9 sec, 0–5 sec, 5–10 sec, and 2.2–2.5 sec for 0.5Hz, 4Hz, 8Hz, and 30Hz frequency components, respectively.)

A time-frequency analysis of the synthesized signal is shown in Figure 24. Here, a time-frequency distribution of the signal is plotted using a short-term Fourier transform (spectrogram). The signal is divided into segments with 256 time points, and a Hanning window is applied to each segment before conducting the Fourier transform. A 50% overlapping between time windows is used. Four peak amplitudes are clearly shown around 0.5Hz, 4Hz, 8Hz, and 30Hz in the frequency axis. The starting and ending time points of each frequency component are also shown in the time axis. The time duration of each frequency component seems to smear in the time axis. For example, the fourth signal component $0.2\sin(2\pi\times 30t)$ in Equation (28) starts at 2.2 seconds and ends at 2.5 seconds. However, the peak amplitude associated with this signal component smeared into a larger area than it should have. The time resolution of this time-frequency analysis can be improved by employing a wavelet analysis.

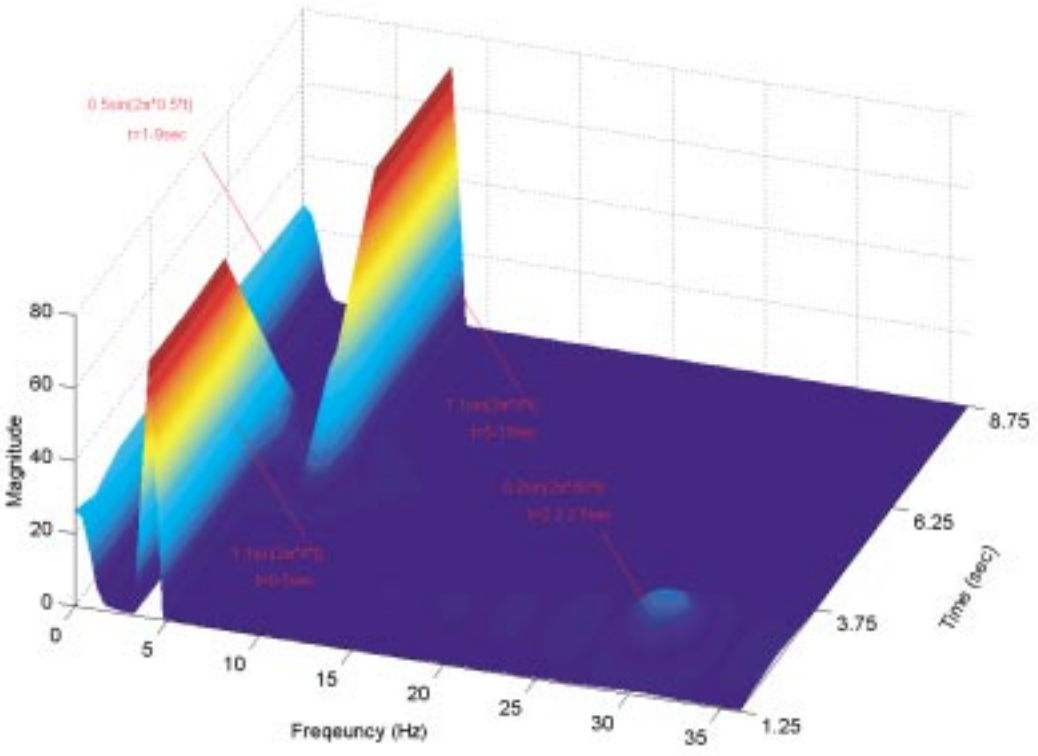

Figure 24: Short-term Fourier transform analysis of the synthesized signal shown in Equation (28) (Time window size=256 points, 50% overlapping, Hanning window applied).

2.7.3 Application to Strain Measurement

Now, the spectrogram analysis is applied to the strain measurement obtained from the fast patrol boat. For the spectrogram analysis, each signal is first split into overlapping segments with a size of 256 points, and a Hanning window is applied to each segment. Fifty percent overlapping is set between two subsequent segments.

Figure 25 shows the spectrogram of Signals 1, 2, and 3, respectively. As stated before, the majority of the response energy is concentrated on the frequency range of 0–5Hz. Particularly, two distinct frequency peaks are observed near 0.5Hz and 3Hz, and there is an energy transmission between these two frequencies. Some fluctuation of the frequency contents with respect to time is also observed. This is an evidence of nonstationarity, and Signal 2 seems to exhibit more severe nonstationarity than the other two signals.

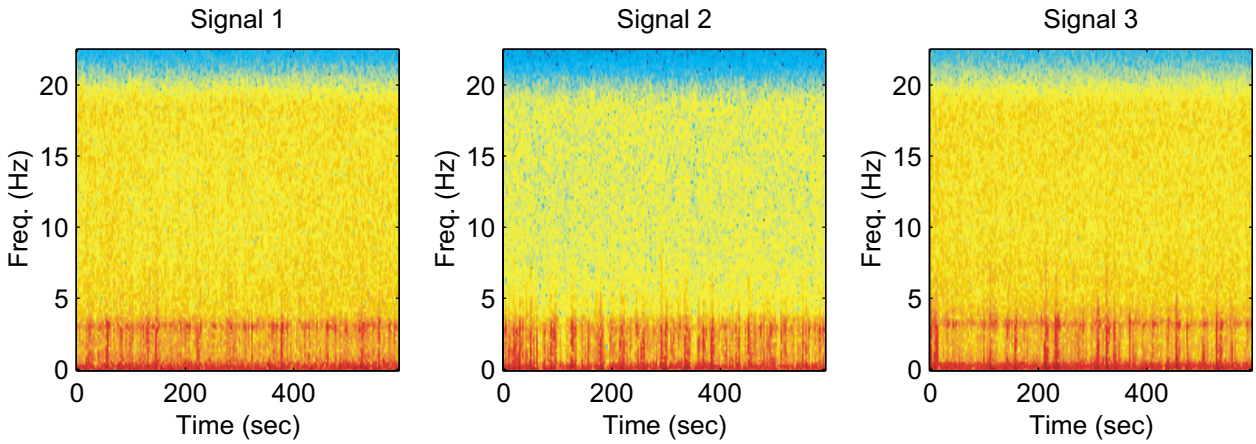

Figure 25: Time-frequency analysis of the normalized time signals.

Next, the spectrogram is computed after all three signals are concatenated together (Signal 1+Signal 2+Signal 3). The spectrogram of the concatenated signal is shown in Figure 26. The distinct transitions of the frequency contents are shown at around 600 seconds and 1200 seconds. Note that these time points (600 and 1200 seconds) correspond to the transition points either from Signal 1 to Signal 2 or from Signal 2 to Signal 3. Again, based on the visual inspection of Figure 25 and Figure 26, Signals 1 and 3 show more similarity than Signals 1 and 2, and the nonstationary nature of Signals 1, 2, and 3 are revealed. Although the visual inspection provided a qualitative means of discriminating signals, it was difficult to draw any useful conclusion based on the visual inspection.

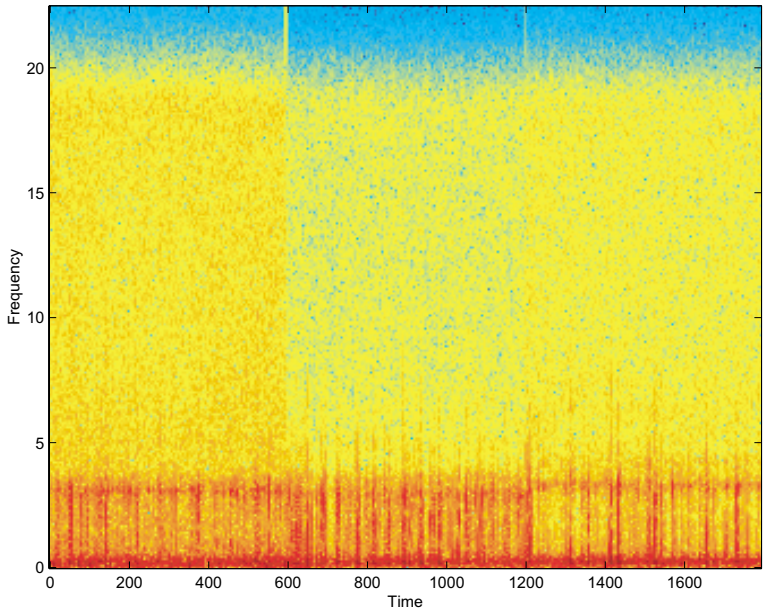

Figure 26: Spectrogram analysis of the concatenated signal.

2.8 AR(Auto-Regressive)-ARX (Auto-Regressive Model with Exogenous Inputs) Analysis

As shown in the previous examples, there is a noticeable difference between Signals 1 and 2. It seems extremely difficult to group Signals 1 and 2 together, and at the same time separate Signal 3 from them. Therefore, a different approach is tried. Here, the additional information that Signals 1 and 2 are obtained from the same structural condition of the system is utilized.

First, each signal is divided into two parts. The first halves of Signal 1 and Signal 2 are employed to generate the "reference database." The second halves of Signal 1 and Signal 2 are later employed for false-positive studies. In this example, signal "blocks" in the reference database are generated by further dividing the first halves of Signal 1 and Signal 2 into smaller segments. These reference signals are considered to be "the pool" of signals acquired from the various operational conditions, but from a known structural condition of the system. (In this example, Signals 1 and 2 are assumed to have been measured under different operational conditions of the surface-effect fast patrol boat. However, it is also known that these two signals correspond to the same structural condition of the system.) When a new signal is recorded (for example, when Signal 3 is measured in this example), this signal is divided into smaller segments, as was done for the blocks in the reference database. Then, the signals in the reference database are examined to find a signal block "closest" to the new signal block. Here, the metric, which is defined as the distance measure of two separate signal segments, is subjective. The detailed formulation of the metric used in this study and the definition of the "closeness" will be described later on.

This approach is based on the premise that if the new signal block is obtained from the same operational condition as one of the reference signal segments and there has been no structural deterioration or damage to the system, the dynamic characteristics of the new signal should be similar to those of the reference signal based on some measure of "similarity." That is, if a time prediction model, such as AR, auto-regressive and moving-average (ARMA), or auto-regressive models with exogenous inputs (ARX), is constructed from the selected reference waveform, this prediction model also should work for the new signal if the signal is "close" to the original. For example, if the second half of Signal 1 is assumed to be a new blind-test signal, the prediction model obtained from the first half of Signal 1 should reproduce the new signal (the second half of Signal 1) reasonably well. On the other hand, if the new signal is recorded under a structural condition different from the conditions where reference signals are obtained, the prediction model estimated from even the "closest" waveform in the reference database should not predict the new signal well. For instance, because Signal 3 is measured under the different structural condition of the system, the prediction model obtained from either Signal 1 or Signal 2 would not predict Signal 3 well even if "similar" waveforms are analyzed. Therefore, the residual errors of the "similar" signals are defined as the damage-sensitive features, and the change of the probability distribution of these residual errors is monitored to detect system anomaly.

In general, a linear time-prediction model cannot capture the dynamic characteristics of nonlinear time series well. To overcome this problem, a "local" modeling approach is employed. Instead of fitting a linear model to the entire time series, the time series is divided into small segments, and a linear model is fit into each local region of the time series. That is, although the local prediction model is linear, the parameters of the linear model adapt to the data in each region of the time series. The procedure is described below in detail.

2.8.1 Procedure

1. All three signals are decimated by a factor of four. This decimation reduces the original sampling rate of the signal, 44.88Hz, to a lower rate, 11.22Hz. The decimation process first filters the signal with an eighth-order lowpass Chebyshev type I filter for better anti-aliasing performance. (The cutoff frequency is set to be $(0.8/R)\acute{}(F_s/2)$. Here, F_s is the original sampling rate, 44.88Hz, and R is the decimation rate, 4.) Then, the decimation process re-samples the resulting filtered signal at the lower rate of 11.22Hz (Oppenheim and Willsky, 1996). Each signal consists of 26980 points with the duration of 601.1667 seconds and results in a sampling rate of 44.88Hz (=26980/601.1667Hz). This sampling rate corresponds to the Nyquist frequency of 22.44Hz. Because the response is mainly observed in the frequency range of 0–5Hz, the signal is re-sampled at every fourth point resulting in the Nyquist frequency of 5.61Hz.

2. Next, an individual signal is divided into two parts. The first halves of Signal 1 and Signal 2 are employed to generate the reference database. Because each signal consists of 6745 (=26980/4) points after decimation, the first half of the signal is now composed of 3372 points. This 3372 point signal is further divided into smaller overlapping segments. The length of a single segment is set to be 1148. (The selection of this segment length is described later.) Therefore, 2225 (=3372–1148+1) overlapping segments are generated from the first half of Signal 1 using a moving time window with 1148 time points. In a similar manner, 2225 segments are obtained from the first half of Signal 2. Therefore, the reference database consists of a total of 4450 signal blocks.

3. Signal 3 is divided into two parts in the same fashion as in Step 2 and assume either the first or second half of Signal 3 as a new data set. In this example, the whole procedure is demonstrated using the second half of Signal 3. The second half of Signal 3 is further divided into three segments. Note that each segment has the same length of 1148 time points as all the reference signal blocks[2].

[2] This calculation of a segment length is rather complicated. As a rule of thumb, the length of a segment is approximately 3372/3≈1148. To be more precise, each segment length is set to be the closest integer to $(3372–q)/3+q$. Here, $q=\max(a,b)+p+1$. Values a, b, and p are defined in Equations (32) and (29), respectively. (In this example, $a=b=5$ and $p=30$. Therefore, $q=36$.) Furthermore, between two consecutive segments, q numbers of points are overlapped. That is, when the second half of Signal 3 is divided into 3 segments, each segment has 1148 time points, and all three segments add to 3372 ($=3\times1148–2\times36$) points.

4. For each segment of the new data, the reference signals are looked up, and the signal segment that is "closest" to the newly obtained one is found. This procedure can be interpreted as a normalization procedure that finds a reference signal segment recorded under a similar "operational" or "environmental" condition as the newly measured one. The "closeness" between two blocks is measured in the following manner.

   4.1. For each segment $x(t)$ from the reference database, construct an AR model with p auto-regressive terms. In this example, an AR(30) is constructed, and an AR(p) model can be written as

$$x(t) = \sum_{j=1}^{p} \phi_{xj} \; x(t-j) \; + e_x(t) \; . \tag{29}$$

   This step is repeated for all 4450 segments in the reference database.

   4.2. Employing a new segment $y(t)$ obtained from the second half of Signal 3, repeat Step 4.1 (Again, segment $y(t)$ has the same length as segment $x(t)$:

$$y(t) = \sum_{j=1}^{p} \phi_{yj} \; y(t-j) \; + e_y(t) \tag{30}$$

   Then, the signal segment $x(t)$ closest to the new signal block $y(t)$ is defined as the one that minimizes the difference of AR coefficients:

$$\text{Difference} = \sum_{j=1}^{p} (\phi_{xj} - \phi_{yj})^2 \; . \tag{31}$$

5. It was assumed that the strain measurements are significantly affected by varying sea states. Therefore, it is necessary to separate the changes in the system response caused by the varying structural conditions from changes caused by varying sea states. It is assumed that the error between the measurement and the prediction obtained by the AR model $e_x(t)$ in Equation (29) is mainly caused by the unknown external input. Based on this assumption, an ARX model (auto-regressive model with exogenous inputs) is employed to reconstruct the input/output relationship between $e_x(t)$ and $x(t)$. (An ARX model is basically identical to an ARMA (Auto-Regressive and Moving-Average) model expect that the input to the ARX model is a known external input rather than white noise.) That is, considering the error term $e_x(t)$ an exogenous input to the system, an ARX(a,b) model is fit to the data to capture the input/output relationship between $e_x(t)$ and $x(t)$. The ARX model is defined as

$$x(t) = \sum_{i=1}^{a} \alpha_i \; x(t-i) \; + \sum_{j=0}^{b} \beta_j \; e_x(t-j) + \varepsilon_x(t) \;\; , \tag{32}$$

where $\varepsilon_x(t)$ is the residual error after fitting the ARX(*a*,*b*) model to the $e_x(t)$ and $x(t)$ pair. The feature for the classification of damage status will later be related to this quantity, $\varepsilon_x(t)$. ARX(5,5) is used in this example. Here, the *a* and *b* values of the ARX model are set rather arbitrarily. However, similar results are obtained for different *a* and *b* values as long as the sum of *a* and *b* is kept smaller than *p* ($a+b \leq p$).

6. Next, an investigation is made to determine how well the ARX(*a*,*b*) model estimated in Equation (32) reproduces the input/output relationship of $e_y(t)$ and $y(t)$:

$$\varepsilon_y(t) = y(t) \; - \sum_{i=1}^{a} \alpha_i \; y(t-i) \; - \sum_{j=0}^{b} \beta_j \; e_y(t-j) \;\; , \tag{33}$$

where $e_y(t)$ is considered to be an approximation of the system input estimated from Equation (30). Again, note that the α_i and β_j coefficients are associated with $x(t)$ and obtained from Equation (32). Therefore, if the ARX model obtained from the reference signal block $x(t)$ was not a good representative of the newly obtained signal segment $y(t)$ and $e_y(t)$ pair, there would be a significant change in the probability distribution of the residual error, $\varepsilon_y(t)$.

7. Finally the ratio of $\sigma(\varepsilon_y)/\sigma(\varepsilon_x)$ is defined as the damage-sensitive feature in this particular example. Here, $\sigma(\varepsilon_y)$ and $\sigma(\varepsilon_x)$ are the estimated standard deviations of $\varepsilon_y(t)$ and $\varepsilon_x(t)$, respectively. If the ratio of $\sigma(\varepsilon_y)/\sigma(\varepsilon_x)$ becomes larger than some threshold value h (>1),

$$\frac{\sigma(\varepsilon_y)}{\sigma(\varepsilon_x)} > \text{h} \;\; , \tag{34}$$

the system is considered to have undergone some structural system changes. However, in order to establish the threshold value, test data need to be acquired under different operational conditions, and the probability distribution of $\sigma(\varepsilon_y)/\sigma(\varepsilon_x)$ first needs to be estimated. Because the data sets provided are limited, the construction of the threshold value based on a rigorous statistical analysis is not achieved in this study.

The proposed AR-ARX approach is summarized below (see Figures 27-33) showing the training quantities in blue and testing quantities in red:

Step 1: Filter all three signals using a low-pass Chebyshev type I filter and resample at a lower sampling rate, R=4.

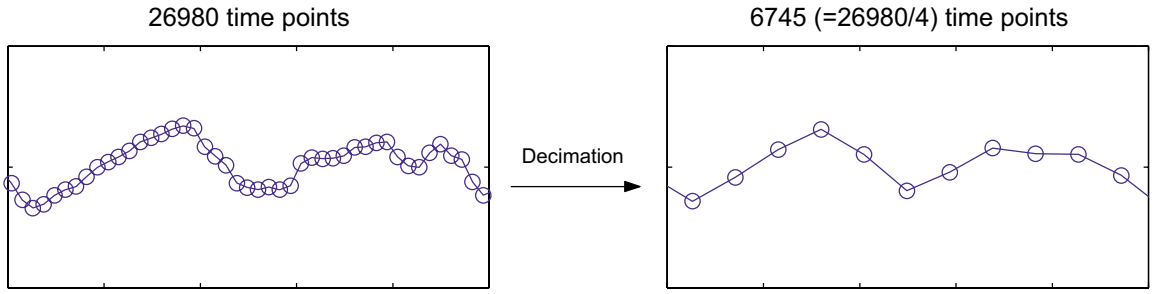

Figure 27: Decimation of all three signals using a low-pass Chebyshev Type I filter and resampling rate, R=4.

Step 2: Divide Signals 1 and 2 into two halves. (The first halves of the signals are used to generate a reference database, and the second halves are used for false-positive studies.)

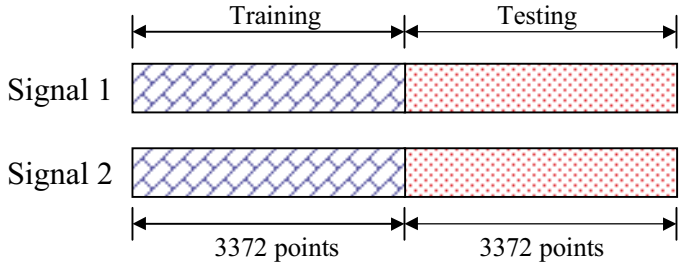

Figure 28: Division of Signals 1 and 2 into training and testing data sets.

Step3: To generate a reference database, further divide the first half of Signal 1 into 2225 overlapping segments with 1148 time points. The first half of Signal 2 is divided in the same way resulting in a total of 4450 segments for the reference database.

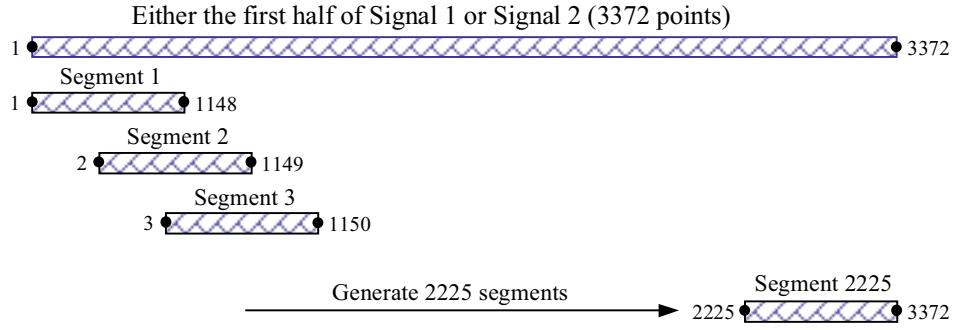

Figure 29: Construction of the reference database from the first halves of Signals 1 and 2.

Step 4: Divide either the first or second half of Signal 3 into three segments with 1148 points.

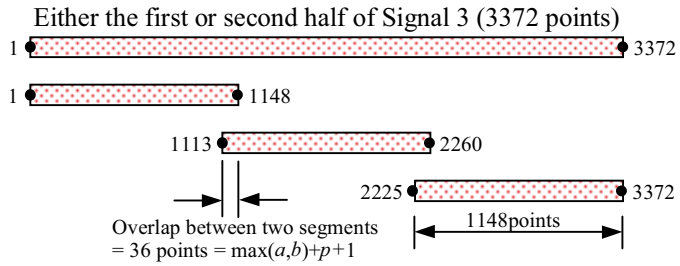

Figure 30: Division of Signal 3 into three segments.

Step 5: Fit AR(30) models to all segments *x(t)* in the reference database and each segment *y(t)* in the test data.

Step 6: For a given test segment *y(t)*, find a segment *x(t)* in the reference database such that the difference in AR coefficients is minimized.

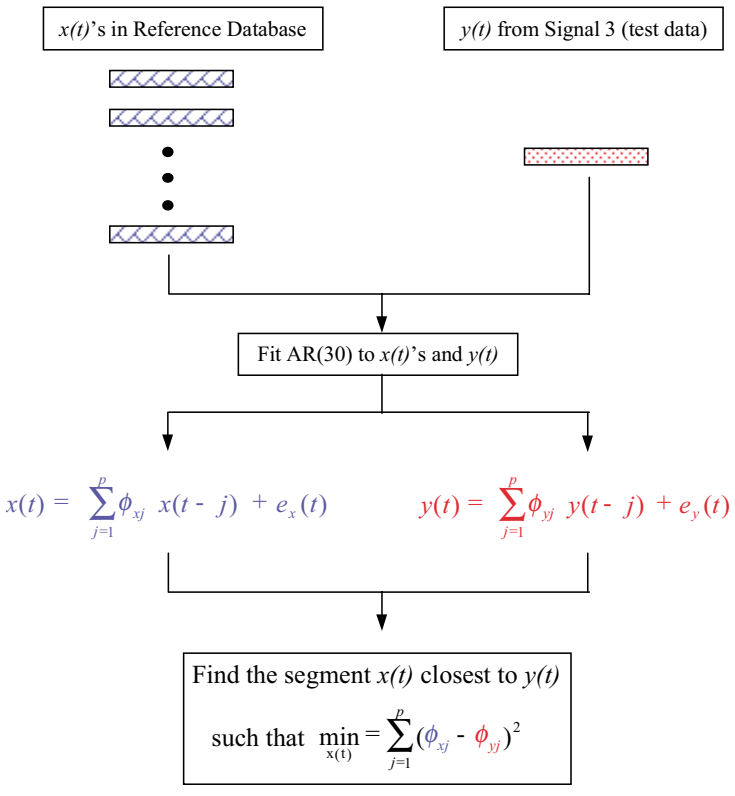

Figure 31: Data Normalization Procedure.

Step 7: Fit an ARX model to the input/output relationship of the $e_x(t)$ and $x(t)$ pair from the segment closest to $y(t)$.

Step 8: Using the ARX coefficients estimated in Step 7, calculate residual errors for the given segment $y(t)$.

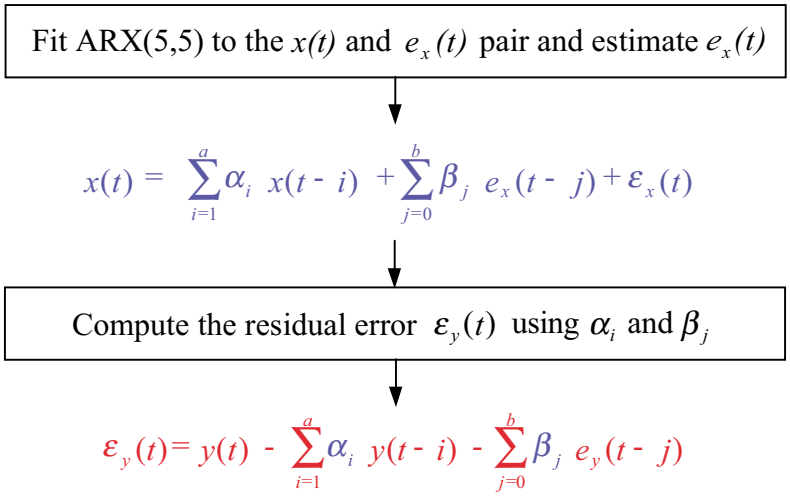

Figure 32: The computation of the residual errors, $\varepsilon_x(t)$ and $\varepsilon_y(t)$.

Step 9: Develop the standard deviation ratio of the residual errors, $\sigma(\varepsilon_y)/\sigma(\varepsilon_x)$.

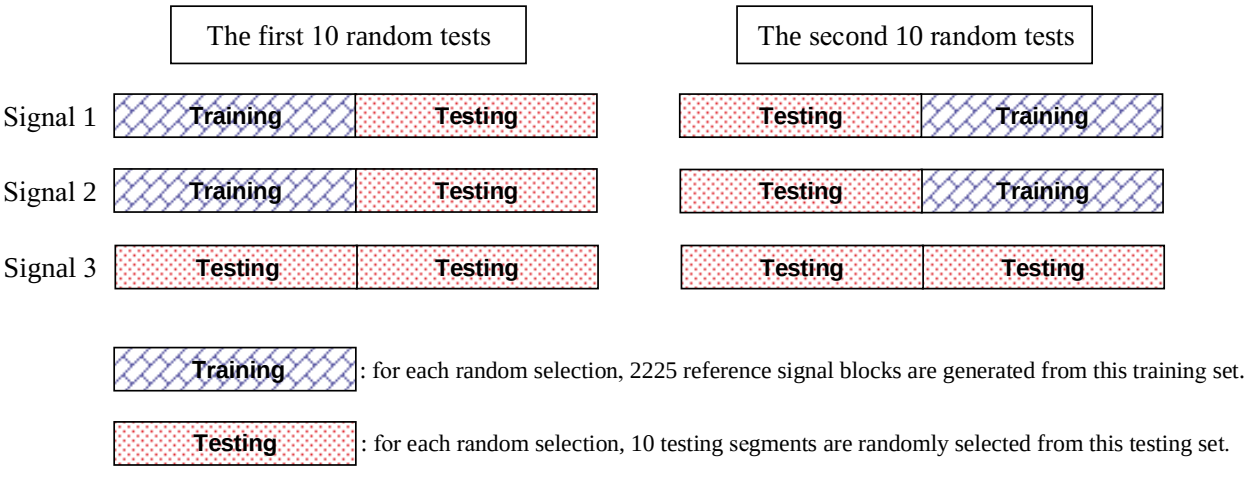

Figure 33: Data generation procedure for 20 random tests.

2.8.2 Application to the Data of Surface-Effect Fast Patrol Boat

The first example is conducted using the first half segments of Signals 1 and 2 as the reference database. Here, the first half of Signal 3 and the second half segments of Signals 1, 2, and 3 are employed as four testing segments with 3372 time points. Figure 34 shows the measured time series of the four testing segments and the corresponding prediction estimated using the ARX (5,5) models as prescribed in Section 2.8.1. In Figure 35, the responses in the range of 100–120 seconds are enlarged for better comparison. Figure 36 displays the corresponding residual errors $\varepsilon_y(t)$ as defined in Equation (33). If the system has experienced a change in structural condition, the standard deviation of new data, $\sigma(\varepsilon_y)$ defined in Equation (34), is expected to increase compared to the standard deviation of the reference signal, $\sigma(\varepsilon_x)$. For example, as shown in the first row of Table 3, $\sigma(\varepsilon_y)$ of the second half of Signal 1 increased about 57% from that of the selected reference signal blocks. (As mentioned earlier, each testing time series consist of 3372 points, and they are further divided into 3 segments with 1148 points. Values $\sigma(\varepsilon_y)$ and $\sigma(\varepsilon_x)$ are computed based on all the residuals obtained from these three segments.) A smaller increase in standard deviation, 26%, is observed for the second half of Signal 2. However, as expected, the standard deviations of the first or second halves of Signal 3 significantly differ from those of the selected reference signals. The standard deviations of the residual errors increased by 126% and 128%, for the first and second halves of Signal 3, respectively. A similar analysis, using the second half segments of Signals 1 and 2 as the reference signals, is presented in the second row of Table 3. In this second example, the first half segments of Signals 1, 2, and 3, and the second half of Signal 3 are employed as testing data sets. Again, a larger value in the $\sigma(\varepsilon_y)/\sigma(\varepsilon_x)$ ratio is found for the residuals from Signal 3 than those from either Signal 1 or Signal 2.

Third, similar tests are repeated 20 times by randomly drawing testing signal blocks from Signals 1, 2, and 3 (see Figure 33). For the first 10 random tests, the first halves of Signals 1 and 2 are used as the reference signals, and 10 testing signal blocks are sampled from each of the first half of Signal 3 and the second half segments of Signals 1, 2 and 3. That is, 4 signal blocks are sampled from Signals 1, 2, and 3 for an individual test. Each signal block consists with 1148 time points as done in the previous examples. Testing blocks for the next 10 tests are collected from the first halves of Signals 1, 2, and 3, and the second half of Signal 3 because the second halves of Signals 1 and 2 are used as the reference signals. To summarize, 20 blocks are sampled from either the first or second half of Signal 1 depending on which portion of Signal 1 is used as part of the reference database. In a similar way, 20 blocks are drawn from Signal 2. An additional 40 blocks are collected from Signal 3 (20 from the first half and another 20 from the second half). The $\sigma(\varepsilon_y)/\sigma(\varepsilon_x)$ ratios for these testing blocks are summarized in Table 4. On average, the 20 testing blocks sampled from

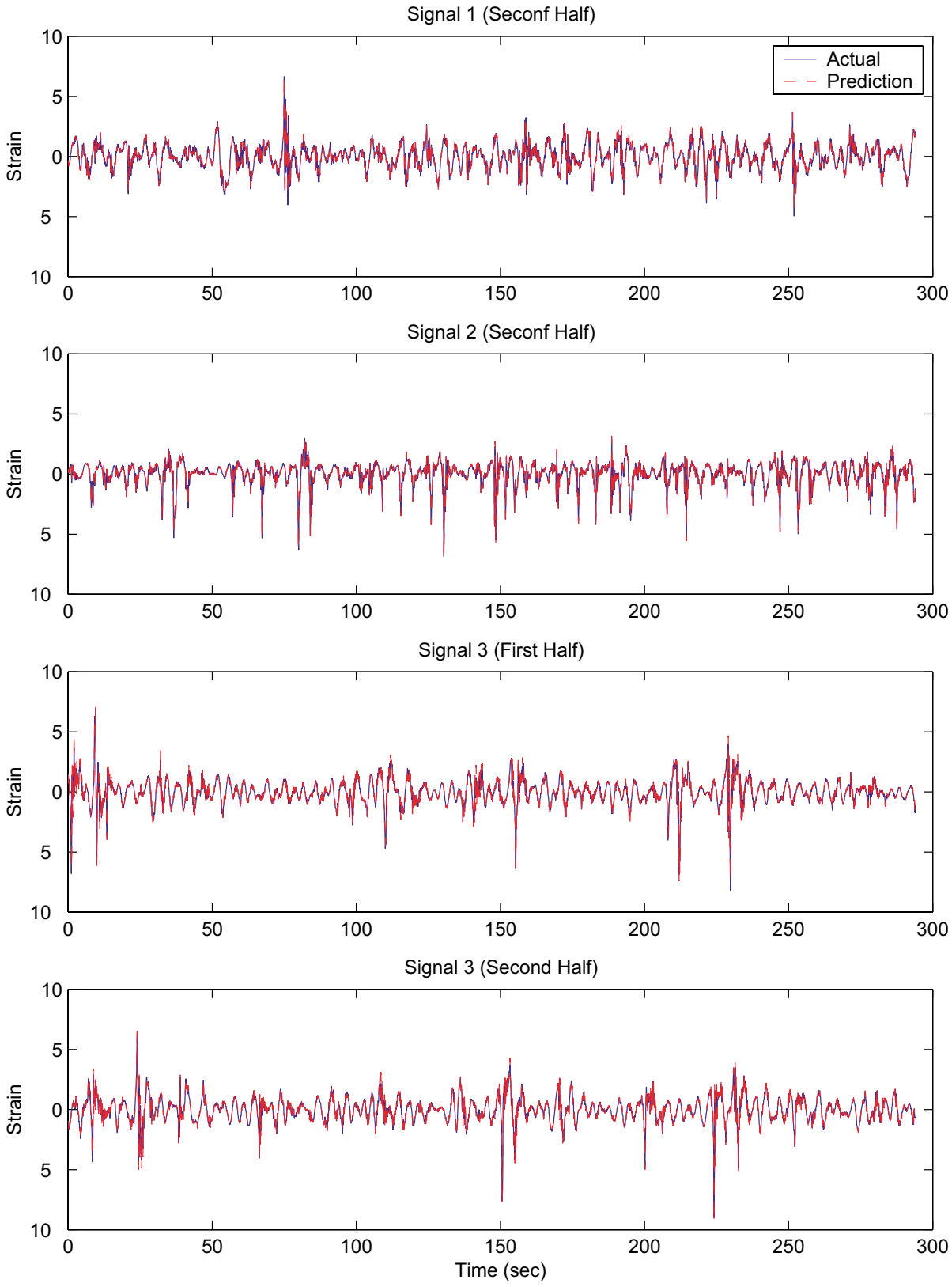

Figure 34: Comparison of the measured vs. predicted signals.

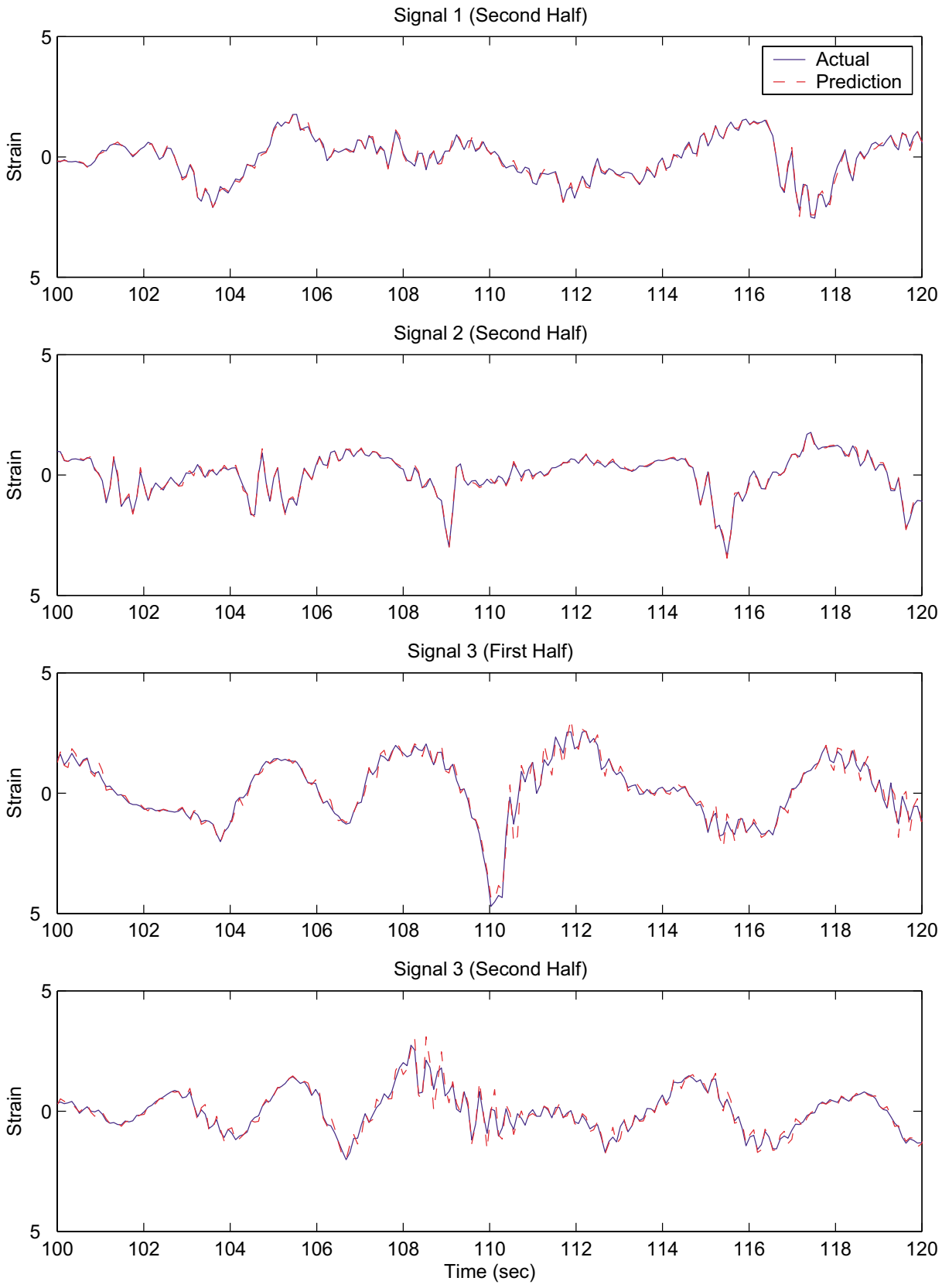

Figure 35: Comparison of the measured vs. predicted signals (zoomed).

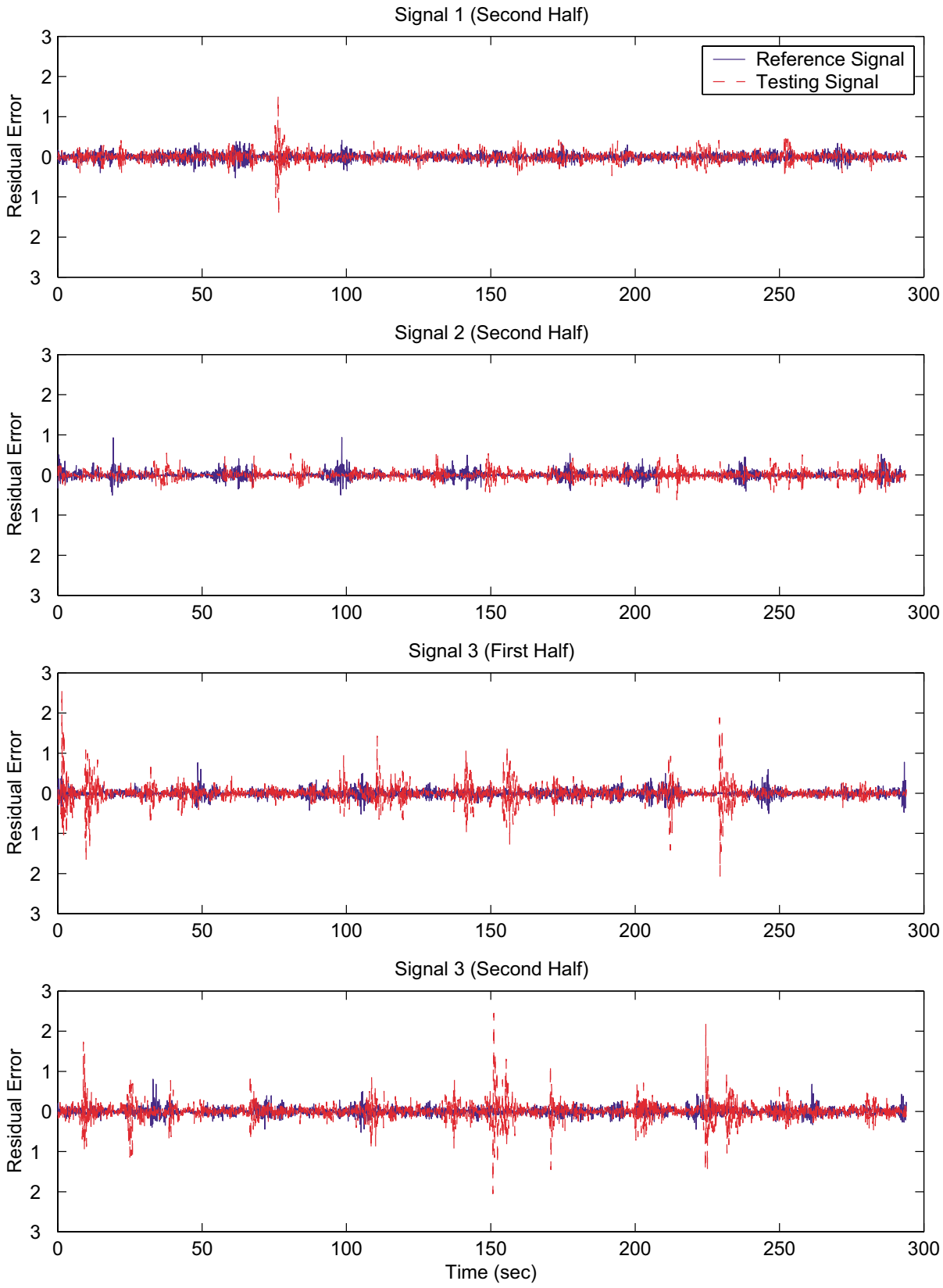

Figure 36: Comparison of residual errors of testing and reference signals.

Table 3: Extracted feature: standard deviation ratio of the residual errors.

Extracted Feature	Signal 1		Signal 2		Signal 3	
	First half	Second half	First half	Second half	First half	Second half
$\sigma(\varepsilon_y)/\sigma(\varepsilon_x)$	reference†	1.5667	reference†	1.2609	2.2625	2.2811
	1.5045	reference†	1.3995	reference†	2.6209	2.5827

† Signal segments with the "reference" notation are used as part of the reference database.

Table 4: The standard deviation ratios for randomly selected signal blocks

Test #	$\sigma(\varepsilon_y)/\sigma(\varepsilon_x)$			
	Sampled from Signal 1	Sampled from Signal 2	Sampled from the 1st half of Signal 3	Sampled from the 2nd half of Signal 3
1†	1.6915	1.1345	2.2173	1.9195
2†	1.2367	1.4677	1.9042	2.0268
3†	1.6073	1.1104	1.9582	2.6095
4†	1.4323	1.5986	2.2655	1.8834
5†	2.0823	1.1347	2.9996	2.1371
6†	1.2297	1.3441	2.3015	2.0779
7†	1.6005	1.1093	2.3700	2.6070
8†	1.8383	1.1276	1.9411	2.5943
9†	1.4310	1.1927	1.7665	2.7302
10†	1.4383	1.6307	1.9356	1.8852
11‡	1.2366	1.1643	2.1586	2.1232
12‡	1.7118	1.6917	2.0868	2.4621
13‡	1.3295	1.4766	2.0961	2.9358
14‡	1.7655	1.7076	2.5354	2.1655
15‡	1.2981	1.8125	2.6723	1.6629
16‡	1.7632	1.7002	1.6828	2.5209
17‡	1.3062	1.2913	2.7374	2.9335
18‡	1.2767	1.8002	2.0038	2.9185
19‡	1.7426	1.6811	1.9682	2.9864
20‡	1.3568	1.4662	2.2023	2.2465
Average	**1.5187**	**1.4321**	**2.1902**	**2.3713**

† The first halves of Signals 1 and 2 are used as the training database, and the testing blocks are sampled from the second halves of Signals 1 and 2.

‡ The second halves of Signals 1 and 2 are used as the training database, and the testing blocks are sampled from the first halves of Signals 1 and 2.

Signal 1 have $\sigma(\varepsilon_y)/\sigma(\varepsilon_x)$ value of 1.5187. The average value for the 20 signals from Signal 2 is 1.4321. On the other hand, the 40 blocks sampled from Signal 3 have much larger increases in standard deviation. The average value is about 2.2808 (= (2.1902+2.3713)/2).

In Figure 37, separation of Signal 3 from Signals 1 and 2 is attempted by setting the threshold value in Equation (34) to be 1.85. This threshold value (h=1.85) results in only 4 misclassifications out of 80 tested cases. That is, 95% of the tested blocks are correctly assigned to their structural conditions. Note that the threshold value employed here is established in rather an *ad hoc* manner. When more test data become available, the threshold value should be established based on a more rigorous statistical approach. However, it was shown that Signal 3 is somehow different from either Signal 1 or Signal 2 employing the additional information that Signals 1 and 2 are obtained from the same structural condition. The same procedure also shows that Signals 1 and 2 are similar. The additional studies with randomly selected testing signals showed no false-positive indication of damage, and discriminate Signal 3 from Signals 1 and 2 with a 95% success rate. It should be noted that the separation of the two structural conditions is conducted in a supervised learning mode because the construction of the threshold value requires the acquisition of data from both of structural conditions.

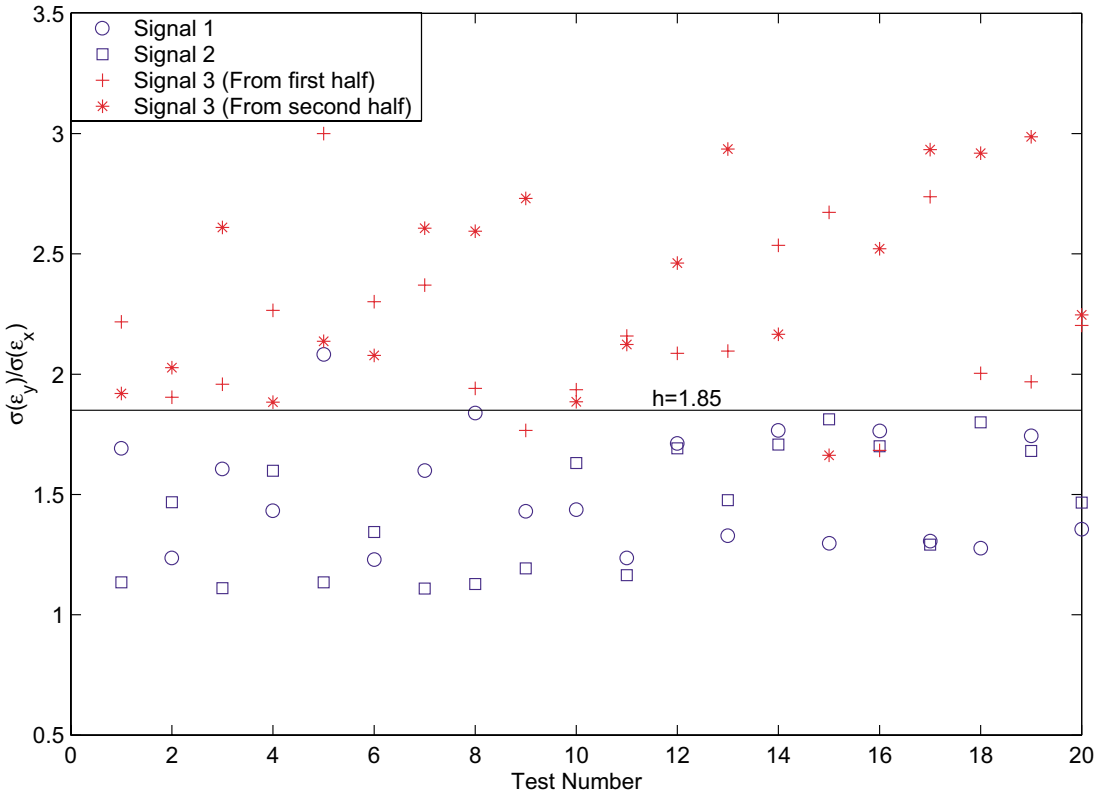

Figure 37: Separation of Signal 3 from Signals 1 and 2 using the ARX residual errors.

2.9 Principal Component Analysis of AR Coefficients

The statistical process control approach in Section 2.5.1 uses the AR model as a means of computing residual errors, which can be considered a univariate feature. However, the AR parameters themselves in Equation (13) can be considered as a multivariate feature that characterizes a given signal.

In order to investigate the AR parameters as a feature, the same decimation and windowing strategy used to generate the moment statistics in Section 2.2 was adopted. A 1000 point window was moved through the time series for each signal, and the parameters for an AR(30) model were extracted. As before, 213 feature vectors were obtained for each signal. The features were concatenated, and a PCA was performed as done before in Section 2.2. For visualization purposes, the projections onto the first two principal components were computed, and the results are plotted in Figure 38. It can be seen that the Signal 3 distribution is distinct from those of Signals 1 and 2. More significantly, the features for one and two show some overlap. Unlike the situation for the moment data, any data interpolating between Signals 1 and 2 would remain distinct from the Signal 3 cluster, so it appears that a good initial feature vector has been found (the AR parameters), and an effective feature extraction process (PCA) has presented itself.

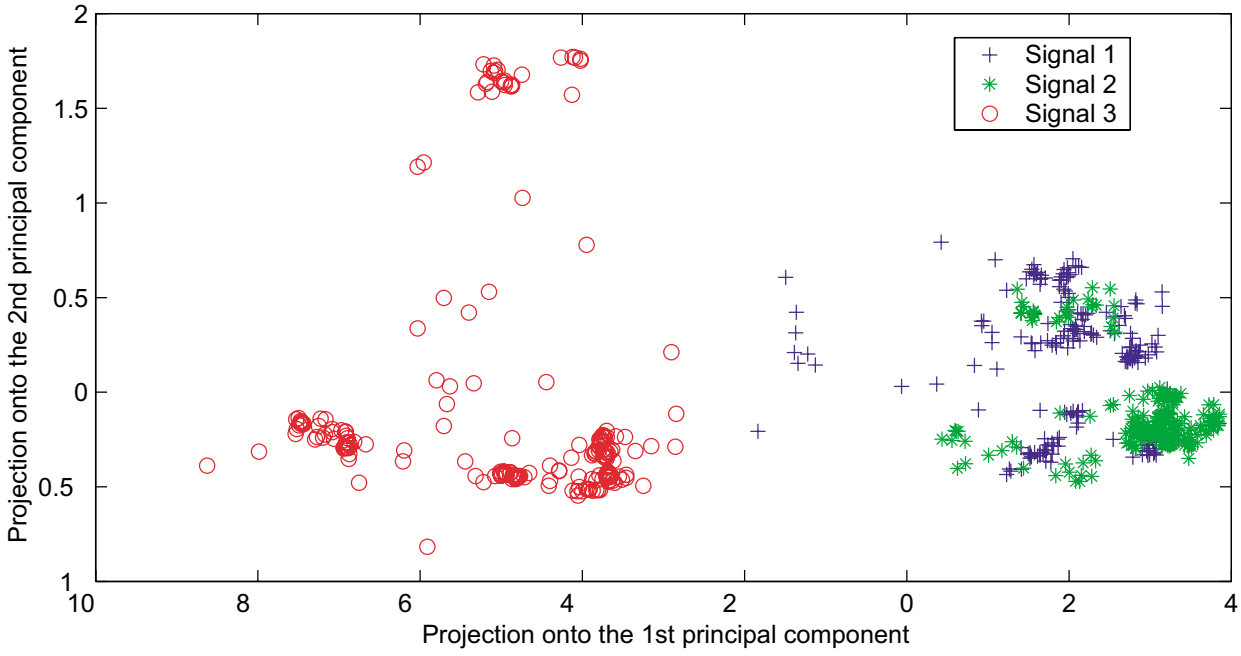

Figure 38: AR parameters for Signals 1 to 3 projected on to the first two principal components.

It is clear from the visualization that the projection onto the first principal component is sufficient to separate Structural Condition 1 (Signals 1 and 2) from Structural Condition 2 (Signal 3). In fact, the first principal component contains 85% of the variance of the initial 30-dimensional set. Figure 39 shows density estimates for the one-dimensional projection for all three signals. A threshold at about –2 is an effective delineator. PCA has provided a single dimensional feature that unambiguously separates Structural Condition 2 from Condition 1.

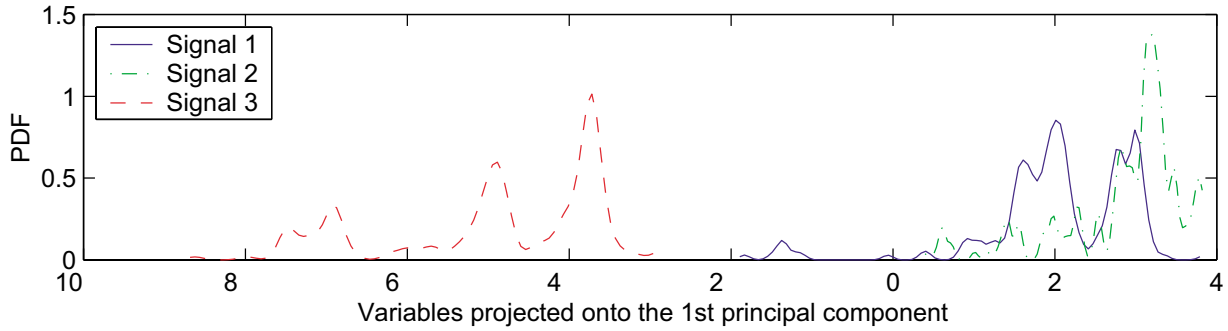

Figure 39: Kernel density estimates of PDFs for signals projected onto the first principal component.

2.10 Outlier Analysis Using AR Coefficients

2.10.1 Outlier Analysis

Outlier analysis and removal has long been a concern of statisticians, and the subject has a large literature. The standard reference, though, is Barnett and Lewis (1994). A study of direct relevance to structural health and condition monitoring can be found in Worden, et al. (2000). As before, only the briefest survey is given here for the sake of completeness.

A *discordant outlier* in a data set is an observation that is surprisingly different from the rest of the data and therefore is believed to be generated by an alternative mechanism. The discordance of the candidate outlier is a measure, which may be compared against some objective criterion. This measure allows the outlier to be judged to be statistically likely or unlikely to have come from an assumed generating model. For damage detection purposes, the generating model is simply the normal condition features of the machine or structure.

The case of outlier detection in univariate data is relatively straightforward in that outliers must “stick out” from one end or the other of the data set distribution. There are numerous discordance tests but one of the most common, and the one whose extension to multivariate data will be employed later, is based on deviation statistics and given by

$$z_\varsigma = \frac{x_\varsigma - \bar{x}}{s} \ , \tag{35}$$

where x_ζ is the potential outlier, and $\bar{x}$ and s are the sample mean and standard deviation, respectively. The latter two values may be calculated with or without the potential outlier in the sample depending upon whether *inclusive* or *exclusive* measures are preferred. This discordance value is then compared to some threshold value and to determine if the observation is an outlier[3].

In general, a multivariate data set consisting of n observations in p variables may be represented as n points in p-dimensional object space. It becomes clear that detection of outliers in multivariate data is more difficult than in the univariate case due to the potential outlier having more "room to hide."

The discordance test, which is the multivariate equivalent of Equation (35), is the Mahalanobis squared distance measure given by

$$D_\varsigma = (\mathbf{x}_\varsigma - \bar{\mathbf{x}})^{\mathrm{T}} \mathbf{s}^{-1} (\mathbf{x}_\varsigma - \bar{\mathbf{x}}) \ , \tag{36}$$

where $\mathbf{x}_\varsigma$ is the potential outlier vector, $\bar{\mathbf{x}}$ is the mean vector of the sample observations, and $\mathbf{s}$ is the sample covariance matrix.

As with the univariate discordance test, the mean and covariance may be inclusive or exclusive measures. In many practical situations the outlier is not known beforehand, and so the test would necessarily be conducted inclusively. In the case of on-line damage detection, the potential outlier is, however, always known beforehand. (It is simply the most recently sampled point). Therefore, it is more sensible to calculate a value for the Mahalanobis squared distance without this observation "contaminating" the statistics of the normal data. Whichever method is used, the Mahalanobis squared distance of the potential outlier is checked against a threshold value, as in the univariate case, and its status determined.

Determination of the rejection threshold is critical. This value is dependent on both the number of observations and the dimension of feature space being selected. A Monte Carlo method was used here to arrive at the threshold value. The procedure for this method was to construct a $p \times n$ (dimension of feature space $\times$ number of observations) matrix with each element being a randomly generated number from a normal distribution with zero mean and a unit variance. The Mahalanobis squared

[3]Here outlier detection is used synonymously with novelty detection. The idea is to associate a new state of the system with the outliers. This use is distinguished from other uses of the outlier analysis in statistics, where the outlier may simply result from a fault in the data capture and be removed in order that it not bias any statistics estimated on the other data.

distances were calculated for all the *p*-vector components, using Equation (36) where $\bar{\mathbf{x}}$ and $\mathbf{s}$ are inclusive measures, and the largest value stored. This process was repeated for at least 1000 trials whereupon the array containing all the largest Mahalanobis squared distances was then ordered in terms of magnitude. The critical values for the 5% and 1% tests of discordance are given by the Mahalanobis squared distances in the array above which 5% and 1% of the trials occur. This process is rather time-consuming and even more so if an exclusive threshold is required; fortunately a simple formula is available that converts inclusive to exclusive thresholds and vice-versa (Barnett and Lewis, 1994).

Note that there is an implicit assumption throughout that the normal condition set has a Gaussian distribution. This assumption will not generally be true. However, if the deviations from the normality are small, i.e., the true distribution is unimodal and has appropriately weighted tails, the outlier analysis may work very well. Considering the data shown in Figure 5, the features from Structural Condition 1 (Signal 1 and 2) would clearly have a bimodal density. It would be possible to use outlier analysis here, but it would give an extremely conservative diagnostic, as a Gaussian with high variance would be needed to adequately cover both clusters. In the case of Figure 5, the fitted Gaussian distribution would almost certainly encompass the features from Signal 3 and would be incapable of showing them to be novel. If the normal condition set is multimodal or deviates significantly from a Gaussian distribution, other methods would be generally used. Possible alternatives include density estimates (Bishop, 1995 and Tarassenko, 1995) or auto-associative networks (Pomerleau, 1993, Worden, 1997).

2.10.2 Application to the Data of Surface-Effect Fast Patrol Boat

The 30-dimensional AR parameters used in Section 2.5.1 were used again for an outlier analysis. The training data were composed of half of Signal 1 and Signal 2. In order to compensate for the nonstationarity of the AR parameter sequence, the training data and testing data were taken alternately from the relevant feature sets. This sampling procedure means that the training data are sampled from the whole time range of the record. The testing data comprised the remaining features from Signals 1 and 2 together with all the features from Signal 3. The resulting outlier statistic is shown in Figure 35. The threshold is the 99.99% confidence threshold; any values above this threshold have a less than 0.01% probability of arising as a random fluctuation on the normal condition set. There is an extremely clear separation between Structural Condition 1 and Structural Condition 2, also note that all points in the testing set from Signals 1 and 2 are well below threshold implying no false-positive indication of change in the structural condition.

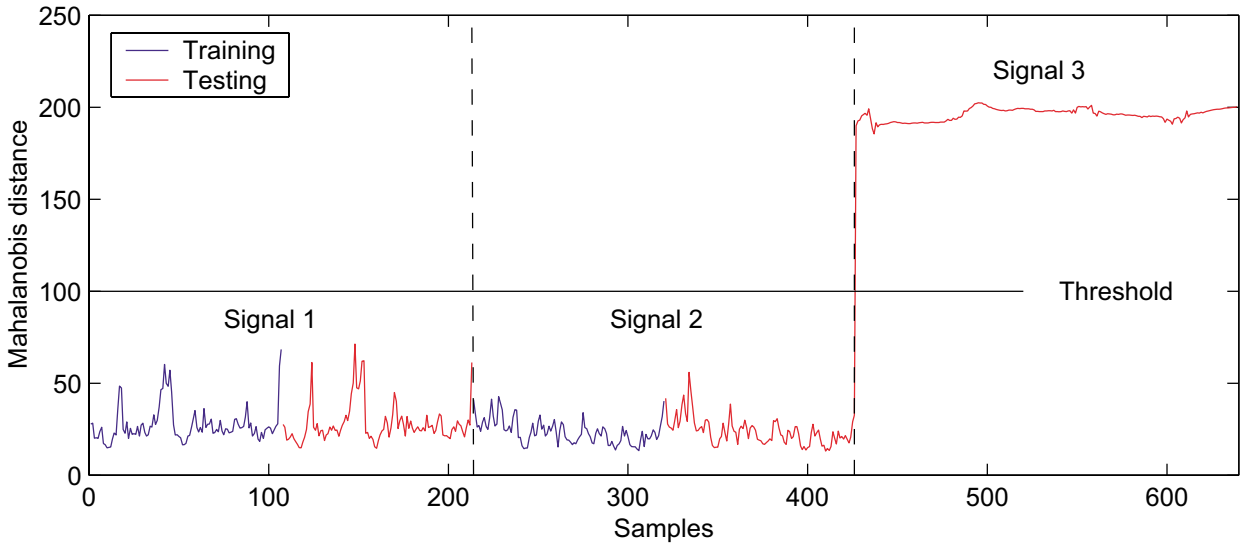

Figure 40: Outlier statistic for Signals 1 to 3.

3 SUMMARY

Staff at NRL provided data corresponding to three time histories measured on a Norwegian surface-effects fast patrol boat with fiber-optic strain gages. They specified that Signal 3 was obtained when the boat was in a different structural condition than when Signals 1 and 2 were obtained. Also, the structural condition was the same when Signals 1 and 2 were obtained. Following LANL's statistical pattern recognition paradigm for structural health monitoring and noting that the operational evaluation and data acquisition portions of this paradigm had been completed by NDRE and NRL, this study tried to identify features from the strain time histories that will distinguish Signal 3 from Signals 1 and 2. These same features must also show that Signals 1 and 2 are not significantly different.

The process of feature extraction began by first looking at statistics of the strain time histories such as mean amplitude, standard deviation, skewness, and kurtosis. Also, probability density estimations were plotted along with Fourier spectra of the signals. Observations of these values or plots showed no consistent trend that could be used to distinguish Signal 3 from Signals 1 and 2. In many cases, features such as the mean value, standard deviation, and kurtosis made it appear that Signal 2 was more similar to Signal 3 than to Signal 1. The plots of the Fourier spectra and the probability density estimates are consistent with the observation that Signal 2 appears more similar to Signal 3. The conclusion from this portion of the analysis was that environmental conditions such as sea states or operational conditions such as the boat speed were making it extremely difficult to distinguish between the two structural states. Finally, the assumption was made that the large number of negative peaks observed in the Signal 2 time history are the result of the boat's hull repeatedly impacting waves. However, there is no way to verify that this assumption is accurate based on the information provided by NRL. Note that the negative peaks observed in Signal 2 manifest themselves in the form of a larger skewness value when compared with the other signals and a corresponding distorted probability density estimation.

An additional analysis of the first four statistical moments was performed using principal component analysis. Two hundred thirteen estimates of these moments were obtained from overlapping windows of the time series data, which were concatenated and decomposed using PCA. The projections onto the first two principal components were then extracted. The moment data showed that the features corresponding to the three signals are separable in the two-dimensional projection. Because PCA is a linear orthogonal transformation, the data must be separable in the original four-dimensional space as well. However, the features for Signal 3 sit between those for

Signals 1 and 2. This observation eliminates the moment statistics as useful features for structural condition assessment. Because Signals 1 and 2 clearly do not represent a full range of the operational and environmental conditions for Structural Condition 1, the clusters corresponding to Signals 1 and 2 are disjointed. For the full range of normal operational and environmental conditions, the features from these data would be expected to interpolate between the features of Signals 1 and 2. This full range of features would overlap substantially with those of Signal 3 making it difficult to classify Signal 3 as novel from those data collected when the boat was in Structural Condition 1.

Next, residual errors between AR models that were fit to the measured strain data and the actual data were used as damage-sensitive features. An auto-correlation analysis was first performed in an effort to estimate the appropriate AR model order so that correlation in the residual errors would be minimized. The AR model was first estimated from a fit to the Signal 1 strain time history. This same model was then used to predict each of the measured strain time-histories and calculate the respective residual errors. As with the analysis of the strain time histories, the basic statistics of the residual errors (mean, standard deviation and kurtosis) showed that the Signal 2 appears to be more closely related to Signal 3 than to Signal 1. A statistical procedure commonly referred to as a control chart was used to further analyze the similarities and differences between the three residual error time-histories. The two control charts that were employed, X-bar and S control charts, examine change in the mean value and standard deviation of the residual errors. Again, the results of this statistical analysis show that Signal 2 appears to be more closely related to Signal 3 than to Signal 1.

The bicoherence and spectrogram were used to qualitatively identify damage-sensitive features. The bicoherence was applied to the strain time histories and the residual error time histories in an effort to identify coupling between frequencies that may be indicative of damage. No consistent trends related to the two structural states could be identified through the qualitative visual inspection of the bicoherence. The spectrogram, which computes a moving-time-window Fourier spectrum, can be used to identify nonstationary system response. Similarly, this analysis did not show any qualitative trends that could be used to distinguish the two different structural conditions.

In an effort to normalize the data and remove operational and/or environmental effects, the residual errors from the AR model were assumed to be primarily related to the unmeasured system input. These residual errors were considered as the input and an auto-regressive model with exogenous inputs (ARX) was fit to the measured strain time-histories. The residual errors from the

ARX model were then used to generate damage-sensitive features. The actual damage-sensitive feature was the ratio of the standard deviations of the residual errors from the similar portions of the two signals being analyzed. A key aspect of this analysis was that the damage-sensitive feature was generated from portions of the various strain time histories that were "similar." Here the similar portion is defined as portions of the signals where the difference in the AR coefficients from the two signals was minimized. This search of a similar signal could be interpreted as a normalization procedure to find a signal portion, which is recorded under a similar operation condition as the newly obtained signal, from the existing database. The feature employed in this study, the standard deviation ratio, showed a clear distinction between Signal 3 and Signals 1 and 2. Also, Signals 1 and 2 appeared to be similar when compared through this feature. To validate the proposed approach, 80 signal segments were randomly sampled for damage classification. Out of 80 tested cases, there were only 4 misclassifications. That is, 95% of the tested signal blocks are correctly assigned to their actual structural conditions. Finally, out of 40 segments obtained from Signals 1 and 2, there was only one false-positive indication of damage, and the rest of 39 cases are correctly assigned to "Structural Condition 1."

The final analysis shown here makes use of outlier analysis in order to separate the two structural conditions. In contrast to the previous analysis in which AR models were used to generate residual errors (univariate features), this procedure used the AR coefficients themselves as multivariate features. The analysis proved very successful in separating Signal 3 from Signals 1 and 2 despite the underlying assumption that the distribution of Structural Condition 1 data was Gaussian. Note that the process of feature extraction also required a number of assumptions. A moving window was passed over the data, and the AR parameters were extracted from each window. The window size and the window overlap are parameters that need to be specified *a priori*, and these specifications should be justified. The window size affects the accuracy to which the AR parameters can be measured, and the window overlap controls the degree of correlation between estimates from adjacent windows in the sequence.

As shown here, there have been a lot of "design parameters" or "knobs" assigned rather arbitrarily throughout this study. Other examples of design parameters include the time window size for spectrogram analysis, the order of AR or ARX models for residual error calculation, the type and order of filtering for decimation, and the choice of a kernel function and a smoothing parameter for kernel density estimation, the subgroup size in control chart analysis, and so on. These design parameters undoubtedly affect the analysis results that were presented in this study,

and the optimum values for these parameters should be sought. However, instead of fully addressing this issue, the design parameters were mainly determined based on previous experience of similar problems and trial-and-errors.

The conclusion from this study is that if the signals are properly normalized, the two different structural conditions can be identified. However, the ability to accomplish this discrimination was highly dependent on *a priori* knowledge that Signal 3 corresponded to a different structural state than that of Signals 1 and 2. Also, the knowledge that Signals 1 and 2 came from the same structural state was necessary to develop the normalization procedure. That is, the discrimination procedure was developed in a *supervised* learning mode. However, the normalization procedure does not require the measure of environmental or operational variations of a system. No need for such measurement becomes a significant advantage for a variety of structures including the fast patrol boat presented here. For example, the ability to measure sea states in the case of the fast patrol boat can be extremely difficult.

It should be pointed out that the procedure developed has only been verified on a limited amount of data. Ideally, it would be necessary to examine many time records corresponding to a wide range of operational and environmental cases as well as different damage scenarios before one could state with confidence that the proposed method is robust enough to be used in practice. Finally, the analyses performed in this study only identify that the structural condition has changed. Analysis of a sensor array is necessary if one is to locate the changing structural condition and, most likely, poses other challenges that have not been encountered in this study.

ACKNOWLEDGEMENT

All members of the Los Alamos Structural Health Monitoring Team contributed to this the study reported herein. The team members include George Papcum and Michael L. Fugate from the Computer, Information, and Communication Group; and Scott Doebling from the Engineering Analysis Group. Funding for this investigation came primarily through Los Alamos National Laboratory's Director's Funded Postdoctoral Fellows Program.

APPENDIX

In this appendix, the theory behind the AR-ARX model presented in the report is briefly summarized, and the advantage of the AR-ARX model over the ARMA model is illustrated using synthetic data.

A.1 ARMA MODEL

A general ARMA model can be represented by the following equation:

$$x(t) = \sum_{i=1}^{a} \alpha_i \; x(t-i) \; + \sum_{j=1}^{b} \beta_j \; \varepsilon(t-j) + \varepsilon(t) \, . \tag{A1}$$

Here a and b are the orders of auto-regressive and moving-average terms, respectively. The value $\varepsilon(t)$ is a unknown white noise process. To estimate the ARMA model, α_i, β_j, and $\varepsilon(t)$ in Equation (A1) need to be estimated simultaneously. This approach generally requires an iterative procedure to solve a general nonlinear optimization. Alternatively, the parameters of the ARMA model can be estimated by a two-stage linear identification process described hereafter (Mayne and Firoozan, 1982).

Hannan and Kavalieris (1984) show that a high-order AR model is able to approximate any ARMA models arbitrarily well. Then, by fitting a high-order AR model to $x(t)$ in Equation (A1), the estimate of the unknown white noise input, $e(t)$, can be obtained:

$$e(t) = \hat{\varepsilon}(t) = x(t) - \sum_{j=1}^{p} \phi_{xj} \; x(t-j) \quad , \tag{A2}$$

where $e(t)(=\hat{\varepsilon}\;(t))$ is the estimate of $\varepsilon(t)$ in Equation (A1). ϕ_{xj} is the auto-regressive term, and p is the order of the AR model. Note that the order of this AR model needs to be larger than the sum of the ARMA orders in Equation (A1). That is, $p \geq a+b$.

Next, an ARX model is formed to estimate the input/output relationship between $e(t)$ and $x(t)$:

$$x(t) = \sum_{i=1}^{a} \alpha_i \; x(t-i) \; + \sum_{j=1}^{b} \beta_j \, e(t-j) + \varepsilon(t) \tag{A3}$$

Now, α_i, β_j, can be obtained by an instrumental variable method (Ljung, 1987). (This instrumental variable method is basically similar to solving simple least squares equations.) For example, if an instrumental variable vector is introduced,

$$\varphi(t) = [x(t-1) \ldots \; x(t-a) \; e(t-1) \ldots e(t-b)]^{\mathrm{T}}. \tag{A4}$$

Equation (A3) becomes

$$\varepsilon(t) = x(t) - \varphi(t)^{\mathrm{T}}\,\theta \ , \tag{A5}$$

where $\theta=[\alpha_1 \ldots \alpha_a\ \beta_1 \ldots \beta_b]^{\mathrm{T}}$.

The least square estimate of θ, which minimizes $\varepsilon(t)$, can be shown to be

$$\hat{\theta} = \mathbf{R}(n)^{-1}\,\mathbf{f}(n) \ , \tag{A6}$$

where

$$\mathbf{R}(n) = \frac{1}{n}\sum_{t=1}^{n} \varphi(t)\ \varphi(t)^{\mathrm{T}} \ \text{ and } \ \mathbf{f}(n) = \frac{1}{n}\sum_{t=1}^{n} \varphi(t)\ x(t) \ . \tag{A7}$$

Therefore, by using a two-step linear approximation procedure (AR-ARX modeling: AR fitting in the first step and ARX estimation in the second step), the parameters of the original ARMA model in Equation (A1) is estimated without solving a complicated nonlinear optimization problem. The ARMA parameters estimated in this two-step approximation can be also used as an initial guess for the following nonlinear optimization. Note that arbitrary initial parameter estimate can converge to a local minimum.

When the ARMA parameters α_i, β_j, and $\varepsilon(t)$ are estimated simultaneously, $\varepsilon(t)$ also becomes a function of the ARMA parameter θ. Then, Equation (A1) can be represented in a similar fashion to Equation (A5)

$$\varepsilon(t,\theta) = x(t) - \varphi(t,\theta)^{\mathrm{T}}\,\theta \ , \tag{A8}$$

where $\varphi(t,\ \theta) = [x(t-1) \ldots\ x(t-a)\ \varepsilon(t-1,\ \theta) \ldots\ \varepsilon(t-b,\ \theta)]^{\mathrm{T}}$.

The objective is to minimize the following quadratic norm of $\varepsilon(t,\ \theta)$ with respect to θ:

$$O(\theta) = \frac{1}{n}\sum_{t=1}^{n} \frac{1}{2}\varepsilon(t,\theta)^2 = \frac{1}{n}\sum_{t=1}^{n} \frac{1}{2}[x(t) - \varphi(t,\theta)^{\mathrm{T}}\,\theta]^2 \ . \tag{A9}$$

Note that because $\varphi(\mathrm{t},\theta)$ is now a function of θ, this object function cannot be minimized by analytical methods. Therefore, the solution is usually sought by the following iterative technique:

$$\hat{\theta}_{i+1} = \hat{\theta}_i - c_i \mathbf{G}_i^{-1} O'(\hat{\theta}_i) \ , \tag{A10}$$

where $\hat{\theta}_i$ denotes the estimate of θ at the ith iteration. The value c_i is a positive constant to control an appropriate decrease in the values of $O(\theta)$. $O'(\hat{\theta}_i)$ is the gradient vector of $O(\theta)$ obtained at $\hat{\theta}_i$. The value $\mathbf{G}_i$ is a directional matrix that modifies the search direction. Depending on the choice of $\mathbf{G}_i$, several minimization methods are available. The simplest choice of $\mathbf{G}_i$ is to take it as the identity matrix, $\mathbf{G}_i=\mathbf{I}$. This choice makes Equation (A10) the gradient or steepest-decent method. Choosing $\mathbf{G}_i=O''(\hat{\theta}_i)$ makes Equation (A10) a Newton method.

A.2 AR-ARX MODEL

As shown in the previous section, an AR-ARX model is basically a linear approximation of an ARMA model. However, the way this AR-ARX model is implemented for damage diagnosis problems makes the proposed AR-ARX approach unique. First, AR models are constructed for a reference signal $x(t)$ and a new signal $y(t)$:

$$x(t) = \sum_{j=1}^{p} \phi_{xj} \ x(t-j) \ + e_x(t) \ \text{ and } \ y(t) = \sum_{j=1}^{p} \phi_{yj} \ y(t-j) \ + e_y(t) \ . \tag{A11}$$

Then, an ARX model is formed with $x(t)$ as output and $e_x(t)$, which is the residual error estimated from the previous AR model, as input:

$$x(t) = \sum_{i=1}^{a} \alpha_i \ x(t-i) \ + \sum_{j=0}^{b} \beta_j \ e_x(t-j) + \varepsilon_x(t) \, . \tag{A12}$$

Finally, the α_i and β_i parameters estimated from the $x(t)$ and $e_x(t)$ pair are used to reproduce the output and input relationship between $y(t)$ and $e_x(t)$:

$$\varepsilon_y(t) = y(t) \ - \sum_{i=1}^{a} \alpha_i \ y(t-i) \ - \sum_{j=0}^{b} \beta_j \ e_y(t-j) \ . \tag{A13}$$

Note that the α_i and β_j coefficients are associated with the reference signal $x(t)$ and are obtained from Equation (A12). Therefore, if the ARX model, obtained from $x(t)$ and $e_x(t)$, were not a good representative of the $y(t)$ and $e_y(t)$ pair, there would be a significant change in the probability distribution of the residual error $\varepsilon_y(t)$ associated with the new signal $y(t)$.

A similar procedure can be applied to the original ARMA model. For example, the α_i and β_j coefficients of an ARMA model can be estimated from the reference signal $x(t)$, and the estimated

ARMA model can be used to predict the new signal $y(t)$. The next section, however, demonstrates that the proposed AR-ARX model is more sensitive to dynamic characteristic changes of a system than the equivalent ARMA model, justifying the use of the AR-ARX model in damage detection problems.

A.3 Comparison of ARMA and AR-ARX Models

To compare the damage diagnosis performance of the AR-ARX and ARMA models, synthetic data sets are generated in this example. First, a reference signal is generated from the following ARMA(2, 2) process:

$$x(t) = 1.5\,x(t-1) - 0.7\,x(t-2) + \varepsilon_x(t) + 1.5\,\varepsilon_x(t-1) + 0.9\,\varepsilon_x(t-2) \tag{A14}$$

An AR-ARX model is then estimated by following the linear approximation procedure described in Section A.1. An ARMA model is also estimated by using the AR-ARX model as an initial guess and solving the nonlinear optimization problem. Figure A1 shows how well the AR-ARX and ARMA models reproduce the reference signal, which is used to construct the model. The white noise input $\varepsilon_x(t)$ is generated from a Gaussian distribution with zero mean and unit standard deviation. Figure A1(a) shows that both AR-ARX and ARMA models successfully reproduce the reference signal. The estimated standard deviation of the prediction error is 1.12 and 1.04 for the AR-ARX and ARMA models, respectively.

Next, these AR-ARX and ARMA models are employed to predict the response of a new signal $y(t)$, which is simulated from the following equation:

$$y(t) = 1.4\,y(t-1) - 0.7\,y(t-2) + \varepsilon_y(t) + 1.5\,\varepsilon_y(t-1) + 1.0\,\varepsilon_y(t-2)\ . \tag{A15}$$

Because the initial ARMA(2, 2) process has changed from Equation (A14) to Equation (A15) (the coefficient of the first auto-regressive term changed from 1.5 to 1.4, and the third moving-average term varied from 0.9 to 1.0), the AR-ARX and ARMA models estimated previously are expected to indicate the system change by increasing the prediction errors. When the AR-ARX model is employed, the standard deviation of the prediction errors, $\sigma(\varepsilon)$, increases from the previous value 1.12 to 25.99 clearly revealing the system change. On the other hand, the $\sigma(\varepsilon)$ values obtained from the ARMA model barely change from 1.04 to 1.10 failing to discover the system change (see Figure A1(b)).

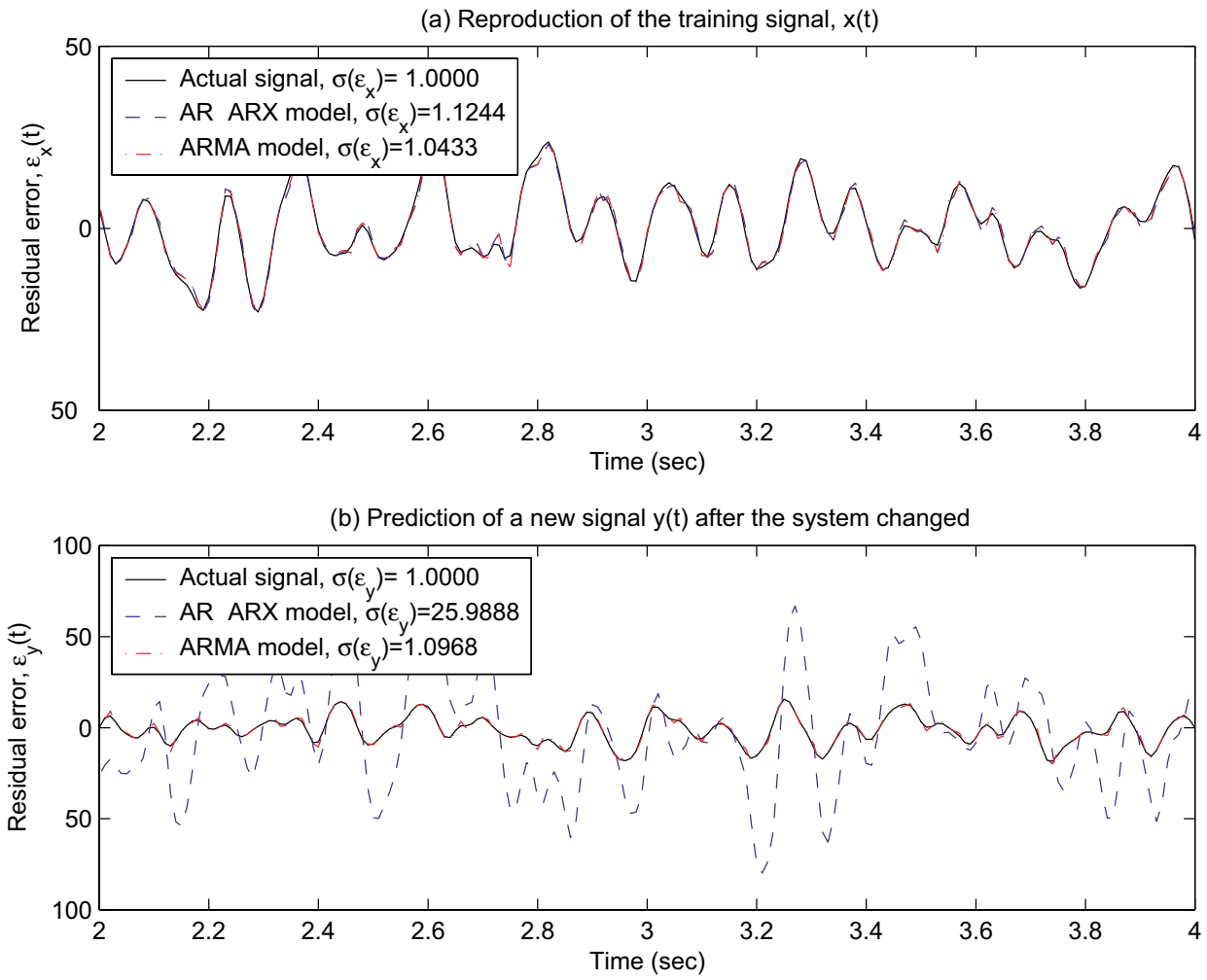

Figure A1: Damage sensitivity comparison of AR-ARX and ARMA models.

While the AR-ARX model tries to predict the input $e_y(t)$ and output $y(t)$ relationship of the new signal using the α_i and β_j coefficients, the ARMA model attempts to reproduce only the output $y(t)$ given the α_i and β_j coefficients. That is, the ARMA has additional flexibilities with the arbitrary input $\varepsilon_y(t)$ making the ARMA model less sensitive to system changes. Therefore, this example illustrates the effectiveness of using the AR-ARX model for damage detection problems.

REFERENCES

1. Barnett, V., and Lewis T., *Outliers in Statistical Data*, Third Edition, John Wiley and Sons, Chichester, UK, 1994.
2. Bishop, C. M., *Neural Networks for Pattern Recognition*, Oxford University Press, New York, 1995.
3. Bowman, A. W., "An alternative method of cross-validation for the smoothing of density estimates," *Biometrika*, **71**, pp. 353–360, 1984.
4. Box, G. E., Jenkins, G. M., and Reinsel, G. C., *Time Series Analysis: Forecasting and Control*, Third Edition, Prentice-Hall, Inc., New Jersey, 1994.
5. Brockwell, P. J., and Davis, R. A., *Time Series: Theory and Methods*, Springer, New York, 1991.
6. Hannan, E. J., and Kavalieris, L., "Multivariate Linear Time Series Models," *Advances in Applied Probability* 16, pp. 492–561, 1984.
7. Jensen, A. E., Taby, J., Pran, K., Sagvolden, G., and Wang, G., "Measurement of global loads on a full scale SES vessel based on strain measurements using networks of fiber optic bragg sensors and extensive finite element analyses," *submitted to Journal of Ship Research*, 2000.
8. Johnson, G. A., Pran, K., Sagvolden, G., Farsund, Ø., Havsgård, G. B., Wang G., Jensen A. E., and Taby J., "Surface effect ship vibro-impact monitoring with distributed arrays of fiber bragg gratings," *Proceedings of the 18th International Modal Analysis*, pp. 1406–1411, Society for Experimental Mechanics, Bethel, CT, 2000.
9. Leuenberger, D. G., *Linear and Nonlinear Programming*, Second Edition, Addison-Wesley, Reading, Massachusetts, 1989.
10. Li, C. J., Ma, J., Hwang, B., and Nickerson, G. W., "Pattern Recognition Based Bicoherence Analysis of Vibrations for Bearing Condition Monitoring," *Sensors, Controls, and Quality Issues in Manufacturing*, American Society of Mechanical Engineers, pp. 1–11, New York 1991.

11. Ljung, L., *System Identifications: Theory for the User*, Prentice Hall, Englewood Cliffs, New Jersey, 1987.
12. Mayne, D. Q., and Firoozan, F., "Linear Identification of ARMA processes," *Automatica* 18, pp. 461–466, 1982.
13. Montgomery, D. C., *Introduction to Statistical Quality Control*, John Wiley & Sons, Inc., New York, 1997.
14. Nikias, C. L., and Petropulu, A. P., *Higher-Order Spectra Analysis: A Nonlinear Signal Processing Framework*, Prentice Hall, Englewood Cliffs, New Jersey, 1993.
15. Oppenheim, A. V., and Willsky, S. H., *Signals & Systems*, Prentice Hall, Englewood Cliffs, New Jersey, 1996.
16. Pomerleau, D. A., "Input reconstruction reliability estimation," in *Advances in Neural Information Processing Systems 5*, editors, S. J. Hanson, J. D. Cowan and C. L.Giles, Morgan Kaufman Publishers, San Mateo, CA, 1993.
17. Pran, K., Johnson, G. A., Jensen, A. E., Hegstad, K. A., Sagvolden, G., Farsund, Ø., Chang, C. C., Malsawma, L., and Wang, G., "Instrumentation of a high-speed surface effect ship for structural response characterization during seatrials," *Proceedings of SPIE's 7th Annual International Symposium on Smart Structures and Materials, Sensory Phenomena and Measurement Instrumentation for Smart Structures and Materials*, pp. 372–379, Society of Photo-Optical Instrumentation, Bellingham, WA, 2000.
18. Rivola, A., and White, P. R., "Bispectal Analysis of the Bilinear Oscillator with Application to the Detection of Fatigue Cracks," *Journal of Sound and Vibration* **216**, pp. 889–910, 1998.
19. Scott, D., *Multivariate density estimation: theory, practice and visualization*, Wiley, New York, 1992.
20. Sharma, S., *Applied Multivariate Techniques*, John Wiley and Son, New York, 1996.
21. Silverman, B. W., *Density Estimation for Statistics and Data Analysis*, Chapman and Hall, New York, 1986.

22. Sohn, H., Fugate, M. L., and Farrar, C. R., "Continuous Structural Monitoring using Statistical Process Control," in *Proceedings of the 18th International Modal Analysis Conference*, Society for Experimental Mechanics, Bethel, CT, 2000.
23. Tarassenko, L., Hayton, P., Cerneaz, Z., and Brady, M., "Novelty detection for the identification of masses in mammograms," *Proceedings of 4th IEEE International Conference on Artificial Neural Networks, Cambridge, UK,* IEEE Conference Publication No. 409, pp. 442–447, New Brunswick, NJ, 1995.
24. Wand, M. P., and Jones, M. C., "Kernel Smoothing," *Monographs on Statistics and Applied Probability,* **60**, Chapman and Hall, New York, 1995.
25. Wang, G., and Pran, K., "Ship hull structure monitoring using fiber optic sensors," *Proceedings of European COST F3 Conference on System Identification & Structure Health Monitoring*, Vol. 1, pp. 15–17, Universidad Politécnica de Madrid, Spain, 2000.
26. Worden, K., "Structural fault detection using a novelty measure," *Journal of Sound and Vibration*, **201**, pp. 85–101, 1997.
27. Worden, K., Manson, G., and Fieller, N. J., "Damage detection using outlier analysis," *Journal of Sound and Vibration*, **229**, pp. 647–667, 2000.

DISTRIBUTION LIST

Masato Abe
University of Tokyo
Dept. of Civil Engineering
Hongo 7-3-1, Bunkyo-ku
Tokyo 113-8656 Japan

Emin Aktan
Drexel University
3201 Arch Street, Suite 240
Philadelphia, PA 19104

Sreenivas Alampalli
New York Dept. of Transportation
1220 Washington Ave.
Albany, NY 12232

Ken Alvin
Sandia National Laboratories
M/S 0439
Albuquerque, NM, 87185-5800

Grahem Archer
School of Civil Engineering
1284 Civil Engineering Building
Purdue University
West Lafayette, IN 47907-1284

Alejandro Asfura
EQE, Inc.
44 Montgomery St., Suite 3200
San Francisco, CA 94104

Bill Baker
Los Alamos National Laboratory
ESA-EA, MS P946
P.O. Box 1663
Los Alamos, NM 87545

Doo Byong Bae
Dept. of Civil and Environmental Eng.
Kookmin University
861-1 Chongnung-dong Songbuk-gu
Seoul,136-702, Korea

Luciana Barroso
CE/TTI Building, Room 705-L
Department of Civil Engineering
Texas A&M University
College Station, TX 77845

Janice Barton
University of South Hampton
Dept. of Ship Science
South Hampton SO17 1BJ
UK

Jim Beck
Applied Mechanics and Civil Engineering
Caltech 104-44
Pasadena, CA 91125

Mrinmay Biswas
Duke University
Dept. of Civil Engineering
Durham, NC 27706

Christian Boller
Daimler Chrysler Aerospace
Munich, D-81663
Germany

James Brownjohn
Nanyang Technological University
School of Civil and Structural Engineering
Nanyang Avenue
Singapore 639798g

Rune Brinker
Department of Building Technology and
Structural Engineering
Aalborg University
Sohngaardsholmsvej 57, DK-9000
Aalborg, Denmark

Bob Burick
Granite Construction Co.
Heavy Construction Division
Box 50024
Watsonville, CA 95077-5024

Thomas Burton
Dept. of Mech. Engineering
Texas Tech University
Lubbock, TX, 79409-1021

R. Cantieni
Uberlandstrasse 129
Dubendorf, CH-8600 Switzerland

Eric Canuteson
Kinemetrics, Inc.
222 Vista Ave.
Pasadena, CA91107

Tom Carne
Dept. 2741
Sandia National Laboratory
Albuquerque, NM 87185-5800

Peter Cawley
Dept. of Mechanical Engineering
Imperial College
Exhibition Rd
London, SW7 2BX
UK

Sung-Pil Chang
Dept. of Civil Engineering
Seoul National University
Shilimdong, Kwanaku,
Seoul, Korea 151-742

Steve Chase
Federal Highway Administration
6300 Georgetown Pike
McLean, VA 22101-2296

Eu Kyeung Cho
Hyundai Engineering &
Construction Co. Ltd.
San1-1, Mabuk-Ri, Goosung-
Myun,Yongin-Si
Kyunggi-Do, Korea, 449-910

Fu-Kuo Chang
Dept. of Aeronautics and Astronautics
Stanford University
Stanford, CA 94305

Tse-Yung Chang
Hong Kong University of Science and Technology
Civil Engineering
Clear Water Bay
Kowloon, Hong Kong

Weiling Chiang
President's Office
National Central University
Chungli, Taiwan

Franklin Cheng
University of Missouri Rolla
Dept. of Civil Eng.
Rolla, MO 65401

Chang Keun Choi
Dep. of Civil Engineering
Korean Institute of Advanced Science and Technology
373-1, Kusong-dong, Yusong-gu,
Taejon ,KOREA, 305-701

Ken Chong
National Science Foundation
4201 Wilson Blvd., Rm. 545
Arlington, VA 22230

Anil Chopra
Earthquake Engineering Research Center
University of California
1301 South 46th St.
Richmond, CA 94804

Leo Christodoulou
DARPA/DSO
3701 N. Fairfax Dr.
Arlington, VA 22203-1714

Lowell Cogburn
Association of American Railroads
P.O. Box 11130
Pueblo, CO 81001

Jerry Conner
Room 1-290
Massachusetts Institute of Technology
77 Massachusetts Avenue
Cambridge, MA 02139

Joel Conte
Dept. of Civil and Environmental Eng.
5731 G Boelter Hall
UCLA
Box 951593
Los Angeles, CA 90095-1593

Roy Craig, Jr.
University of Texas at Austin
Aerospace Engineering and Engineering
Mechanics Dept., Mail Code C0600
Austin, TX 78712Ð1085

Tim Darling
Los Alamos National Laboratory
MST-10, MS K764
P.O. Box 1663
Los Alamos, NM 87545

Barry Davidson
Compusoft Engineering Ltd.
PO Box 9493
Newmarket, Auckland
New Zealand

Shirley Dyke
Washington University
One Brookings Hall 1130
St. Louis, MO 63130

Dave Ewins
Imperial College
Mechanical Engineering Dept.
Exhibition Road
London SW7 2BX, UK

Gregory Fenves
Department of Civil and Environmental
Engineering, MC 1710
University of California
Berkeley,CA 94720-1710

M. Ferner
Anlauf Ingenicur - Consulting GMBH
Posttach 101259
D-69002 Heidelberg, Germany

Mike Friswell
Dept. of Mechanical Engineering
University of Wales, Swansea
Singleton Park,
Swansea, SA2 8PP
UK

Claus-Peter Fritzen
Institute of Mechanics and Automatic Control
University of Siegen
Paul-Bonatz-Str. 9-11
D-57068 Siegen, Germany

Gongkang Fu
New York State Dept. of Transportation
1220 Washington Ave.
Albany, NY 12232

Chris Gannon
Penguin Engineering Ltd
PO Box 33 093
Petone, New Zealand

Ephrahim Garcia
DARPA
Dense Science Office
3701 N. Fairfax Dr.
Arlington, VA 22203-1714

Luigi Garibaldi
Dipartimento di Meccanica
Politecnico di Torino
Corso Duca degli Abruzzi, 24
10129 Torino, Italy

Lothar Gaul
Institut A fur Mechanik
Universitat Stuttgart
Pfaffenwaldring 9
70550 Stuttgart, Germany

Michael Grygier
NASA Johnson Space Center
ES43
Houston, TX 77058

Alfredo Guemes
UPM
ETSI Aeronautics
Madrid, 28016
Spain

Joe Hammond
Inst. of Sound and Vibration Research
University of South Hampton
SO17 1BJ
South Hampton, UK

Kurt Hansen
Dept. of Energy Engineering
Technical University of Denmark
Building 404, DTU
DK 2800 Lyngby
Denmark

Nicholas Haritos
Dept. of Civil and Environment Eng.
University of Melbourne
Parkville, Victoria 3052
Australia

Phil Hashimoto
300 Commerce Drive
Suite 200
Irvine, CA 92602

Dan Inman
Virginia Polytechnic Institute of State Univ.310
New Engineering Building
Mail code 0261
Blacksburg, VA 24061-0219

Jeong Hwan Jang, Ph.D.
EJTECH CO. LTD.
5th Floor, Seoweon Building, 2-44
YangJae-Dong, Seocho-Gu, Seoul, Korea

Jim Johnson
EQE, Inc.
44 Montgomery St., Suite 3200
San Francisco, CA 94104

Tarsem Jutla
Caterpillar, Inc.
Technical Center, Bldg. K
P.O. Box 1875
Peoria, Illinois 61656-1875

Daniel Kammer
University of Wisconsin-Madison
Dept. of Engr. Mech. and Astronautics
3352 Engr. Hall, 1415 Johnson Drive
Madison, WI 53706

Tom Kashanganki
University of Maryland
SMART Materials and Structures Res. Center
College Park, MD 20742

Robert Kennedy
18971 Villa Terrace
Yorba Linda, CA 92686

Klaus Kerkhoff
Staatliche Materialprufungsanstalt
Universitat Stuttgart
D-70569 Stuttgart (Vailhingen)
Germany

Magdi Khalifa
University of Nebraska Lincoln
Civil Engineering Department
W348 Nebraska Hall
Lincoln, NE 68588-0531

Chul Young Kim
Dept. of Civil & Environmental Engineering
Myong Ji University
San 38-2, Nam-dong, Yongin-si
Kyunggi-do, 449-728, Korea

Hyoung-Man Kim
McDonnell Douglas Aerospace
M/S: MDC-2-3353
13100 Space Center Blvd
Houston, TX 77059

Jae Kwan Kim
Dept. of Civil Engineering
Seoul National University
Shilimdong, Kwanaku,
Seoul, Korea 151-742

Nam Sik Kim
Hyundai Eng. & Construction Co. Ltd.
San1-1, Mabuk-Ri, Goosung-
Myun,Yongin-Si
Kyunggi-Do, Korea, 449-910

Anne Kiremidjian
Stanford University
Department of Engineering
Terman Engineering Center 238
Stanford, CA 94305-4020

Poul Kirkegaard
Department of Building Technology and
Structural Engineering
Aalborg University
Sohngaardsholmsvej 57, DK-9000
Aalborg, Denmark

Hyun Moo Koh
Dept. of Civil Engineering
Seoul National University
Shilimdong, Kwanaku,
Seoul, Korea 151-742

Richard Kohoutek
University of Wollongong
Dept. of Civil and Mining Engineering
Northfields Avenue
Wollongong 2522 Australia

John Kosmatka
University of California
Department of AMES
San Diego, CA 92093-0085

Christian Kot
Argonne National Laboratory
9700 South Cass Ave. RE/331
Argonne, IL 60439-4817

Everett Kuo
Ford Research Laboratory
P.O. Box 2053/MD2122
Dearborn, MI 48121

Charles Larson
Boeing
MS.H013-C326
5301 Bolsa Avenue
Huntington Beach, CA 92649

Kincho Law
Dept. of Civil Engineering
Stanford University
Stanford, CA 94305-4020

George Lee
Multidisciplinary Center for Earthquake
Engineering Research
SUNY at Buffalo
Red Jacket Quadrangle
Buffalo, NY 14261-0025

H. S. Lew
NIST
Bldg. 226, Rm B168
Gaithersburg, MD 20899

Brett Lewis
APTEK, Inc.
1257 Lake Plaza Dr.
Colorado Springs, CO 80906

Zhong Liang
University of Buffalo
Dept. of Mechanical and Aerospace Eng.
141 Ketter Hall
Buffalo, NY 14260

Nick Lieven
Dept. of Aerospace Engineering
University of Bristol, Queen's Bldg.
Bristol, BS8 1TR, UK

Tae W. Lim
University of Kansas
Dept. of Aerospace Engineering
2004 Learned Hall
Lawrence, KS 66045

Michael Link
Universitat Gesamthochschule Kassal
Fachbereich 14
Bauingenienurwesen, Fachgebiet Leichtbau
Monchebergstr. 7
D-34109 Kassal
Germany

Shih-Chi Liu
National Science Foundation
4201 Wilson Blvd.
Arlington, VA 22230

Richard Livingston
Federal Highway Administration
6300 Georgretown Pike, HRD1-12
McLean, Va 22101

Nuno Maia
IDME/IST
Av. Rovisco Pais
1096 Lisboa Codex
Portugal

Dave Martinez
Sandia National Laboratories
M/S 0439
Albuquerque, NM, 87185-5800

Sami Masri
University of Southern California
Department of Civil Engineering
MC 2531
Los Angeles, CA 90089-2531

Randy Mayes
Sandia National Laboratories
MS0557
PO Box 5800
Albuquerque, NM 87185

David McCallen
Center for Complex Distributed Systems
Lawrence Livermore National Laboratory
Livermore, CA 94550

Ken McConnell
Iowa State University
3017 Black Eng. Bldg.
Ames, Iowa 50011

Albert Migliori
Los Alamos National Laboratory
MST-NHMFL, MS E536
P.O. Box 1663
Los Alamos, NM 87545

Akira Mita
Graduate School of Science and Technology,
Keio University
8-14-1 Hiyoshi, Kohoku-ku
Yokohama 223-8522
Japan

Jack Moehle
University of California
Department of Civil Engineering
775 Davis Hall
Berkeley, CA 94720

Julio M. Montalvao e Silva
IDME/IST
Av. Rovisco Pais
1096 Lisboa Codex
Portugal

Denby Morrison
Shell E&P Technology Company
Ocean R&D, Bellarie Technology Center
P.O. Box 481
Houston, TX 7700

Peter Moss
University of Canterbury
Department of Civil Engineering
Private Bag 4800
Christchurch, New Zealand

John Mottershead
Dept. of Engineering
Brownlow Hill
University of Liverpool
Liverpool, L69 3GH
UK

Robert Murray
Lawrence Livermore National Laboratory
P.O. Box 808, L-197
Livermore, CA 94550

H.G. Natke
Universtat Hannover
Applestrabe 9A
D-30167 Hannover
Germany

Robert Nigbor
Department of Civil Engineering
University of Southern California
Los Angeles, CA 90089-2531

Ozden Ochoa
Offshore Technology Research Center
1200 Mariner Dr.
Texas A&M University
College Station, TX 77845

Wally Orisamolu
Manager, Structural Integrity &
Reliability Group
Components Department
United Technologies Research Center
411 Silver Lane, MS 129-73
East Hartford, CT

Roberto Osegueda
The University of Texas at El Paso
Department of Civil Engineering
El Paso, TX 79912
Richard Pappa
NASA Langley Research Center
MS 230
Hampton, VA 23681

Gerard Pardoen
University of California-Irvine
101 ICEF-Civil Eng.
Irvine, CA 92717

K. C. Park
Center for Aerospace Structures
University of Colorado, Boulder
Campus Box 429
Boulder, CO 80309-0429

Lee Peterson
Center for Aerospace Structures
University of Colorado, Boulder
Campus Box 429
Boulder, CO 80309-0429

Darryll J. Pines
Dept. of Aerospace Engineering
Room 3154 Engineering Classroom Bldg
University of Maryland
College Park, MD 20742

Bruno Piombo
Departimento di Meccanica
Politecnico di Torino
Corso Duca degli Abruzzi, 24
I - 10129 Torino, Italy

Bob Randall
School of Mechanical/Manufacturing Engineering
University of New South Wales,
Sydney 2052
Australia

John Reed
922 Parma
Los Altos, CA 94024

Mark Richardson
Vibrant Technology, Inc.
18141 Main Street
Jamestown, CA 95327

Jim Ricles
Lehigh University
Department of Civil Engineering
117 ATLSS Drive, H Building
Bethlehem, PA 18015-4729

Rolf Rohrmann
Federal Institut for Materials Research and Testing (BAM)
Laboratory Geotechnique and
Structural Dynamics
Unter den Eichen 87
12205 Berlin
Germany

John Ruminer
Los Alamos National Laboratory
DDESA, MS P945
P.O. Box 1663
Los Alamos, NM 87545

Romualdo Ruotolo
Dip. Ingegneria Aeronautica e Spaziale
Politecnico di Torino
10100 Torino
Italy

Anders Rytter
RAMBOLL
Kjaerulfsgade 2
DK-9400 Norresundby
Denmark

Erdal Safak
U.S. Geological Survey
DFC, Box 25046, MS.966
Denver, CO 80225

M. Saiidi
College of Engineering
Department of Civil Eng./258
Reno, NV 89557-0152

Masoud Sanayei
Tufts University
Dept. of Civil and Env. Engineering
Medford, MA 02155

Jose Maria Campos dos Santos
UNICAMP
Caixa Postal 6122
13083-970 Campinas, SP
Brazil

Paul Sas
Katholieke Universiteit Leuven
Mechanical Engineering Dept.
Celestijnenlaan 300B
B-3001 Herverlee
Belgium

Bob Shumway
Division of Statistics
Univ. of California, Davis
Davis, CA 95616

Michael Simmons

Caterpillar, Inc.
Technical Center, Bldg. A
P.O. Box 1875
Peoria, Illinois 61656-1875

Suzanne Smith
University of Kentucky
Department of Engineering Mechanics
467 Anderson Hall
Lexington, KY 40506-0046

Cecily Sobey
Earthquake Engineering Research Center
Library
Gift & Exchange Dept.
University of California/RFS 453
1306 South 46th Street
Richmond, CA 94804-4698

Norris Stubbs
Texas A&M University
Department of Civil Engineering
Mechanics & Materials Center
College Station, TX 77843-3136

Fred Tasker
Dept. of Mechanical Engineering
University of Maryland Baltimore County
Baltimore, MD 21228-5398

Mike Todd
Naval Research Laboratory
Optical Sciences Division
Code 5673
4555 Overlook Ave. SW
Washington D.C. 20375

Geoff Tomlinson
The University of Sheffield
Department of Mechanical and Process
Engineering
PO Box 600
Mappin St
Sheffield S1 4DU UK

Pavel Trivailo
RMIT University
226 Lorimer St.
Fishermen's Bend 3207 Victoria
GPO Box 2476V
Melbourne 3001 Victoria Australia

Wen S. Tseng
International Civil Engineering Consultants,
Inc. (ICEC)
1995 University Ave., Suite 119
Berkeley, CA 94704

Ward Turner
Exxon Production Research Company
P.O. Box 2189
Houston, TX 77252

Herman Van Der Auweraer
LMS International
Interleuvenlaan 68
B-3001 Leuven, Heverlee
Belgium

C. E. Ventura
The University of British Columbia
Dept. of Civil Engineering
2324 Main Mall
Vancouver, B.C.
Canada, V6T 1Z4

Sara Wadia-Fascetti
Northeastern University
Dept. of Civil Engineering
443 Shell Engineering Center
Boston, MA 02115

Gunnar Wang
Norwegian Defense Research Est.
P.O. Box 25
N-2007 Kjeller, Norway

Ming Wang

Dept. of Civil and Material Engineering (M/C 246)
College of Engineering
842 West Taylor St.
Chicago, Illinois 60607-7023

Semyung Wang
Visiting Research Scholar
Aerospace System Design Lab
School of Aerospace Engineering Technology
Georgia Institute of Technology
Atlanta, GA 30332-0150

Lloyd Welker, Jr.
Ohio Department of Transportation
25 South Front Street
Columbus, OH 43216-0899

Robert West, Jr.
Virginia Polytechnic Institute of State Univ.
Structural Imaging and Modal Analysis Lab.
Mechanical Engineering Department
Blacksburg, VA 24061-0238

Ed White
Boeing
P.O. Box 516
St. Louis, MO 63166

Ken White
Dept. of Civil, Agricultural, and Geological Eng.
Box 30001/Dept. 3CE
Las Cruces, NM 88003-0001

Al Wicks
Mechanical Engineering Department
Virginia Tech. Univ.
Blacksburg, VA 24061-0238

P. Winney
P&P Engineering
Consultant Engineers
P.O. Box 36
Billingshurst, West Sussex RH14 OYG

Felix S. Wong
Weidlinger Associates
4410 El Camino Real, Suite 110
Los Altos, CA 94022-1049

Shi-Chang Wooh
Room 1-272
Massachusetts Institute of Technology
77 Massachusetts Avenue
Cambridge, MA 02139

Keith Worden
The University of Sheffield
Department of Mechanical and Process Engineering
PO Box 600
Mappin St
Sheffield, S1 3JD UK

Fan Wu
Risk Management & Solutions, Inc.
149 Commonwealth Drive
Menlo Park, CA 94025

J. T. P. Yao
Dept. of Civil Engineering
Texas A&M University
College Station, TX 77843-3136

Chung-Bang Yun
Dept. of Civil Engineering
Korean Institute of Advanced Science and Technology
373-1, Kusong-dong, Yusong-gu,
Taejon, KOREA, 305-701

Los Alamos
NATIONAL LABORATORY

Los Alamos, New Mexico 87545